

**Target Motion Analysis Using
Range-only Measurements:
Algorithms, Performance and
Application to Ingara ISAR Data**

B. Ristic, S. Arulampalam and
J. McCarthy

DSTO-TR-1095

DISTRIBUTION STATEMENT A

Approved for Public Release

Distribution Unlimited

20010404 162

Target Motion Analysis Using Range-Only Measurements: Algorithms, Performance and Application to Ingara ISAR Data

B. Ristic, S. Arulampalam and J. McCarthy

Surveillance Systems Division
Electronics and Surveillance Research Laboratory

DSTO-TR-1095

ABSTRACT

The report considers the problem of target motion analysis from range and range-rate target measurements. The motivation for this work comes from the need to track the target motion with the Ingara Multi-Mode Radar during an extended data collection in the ISAR mode. The report makes three main contributions. First, the theoretical Cramér-Rao bound for the performance of an unbiased range-only tracking algorithm is derived. Second, three algorithms for target motion analysis (using range and range-rate measurements only) are developed and compared to the theoretical bounds of performance. The three algorithms are: the Maximum Likelihood estimator, the Extended Kalman filter and the Regularised Particle filter. Finally, the report presents the results of the application of the developed theory to the ISAR data collected in the recent trials with the Ingara radar.

APPROVED FOR PUBLIC RELEASE

DEPARTMENT OF DEFENCE
DEFENCE SCIENCE & TECHNOLOGY ORGANISATION | **DSTO**

AQ FOL-07-1138

Published by

DSTO Electronics and Surveillance Research Laboratory

PO Box 1500

Salisbury, South Australia, Australia 5108

Telephone: (08) 8259 5555

Facsimile: (08) 8259 6567

© Commonwealth of Australia 2001

AR No. AR-011-693

January 2001

APPROVED FOR PUBLIC RELEASE

Target Motion Analysis Using Range-Only Measurements: Algorithms, Performance and Application to Ingara ISAR Data

EXECUTIVE SUMMARY

The report investigates the problem of target motion analysis from range and range-rate measurements. The problem is of importance for tracking surface vessels while collecting data in the ISAR mode of the Ingara multi-mode radar. The report derives the bounds of performance and considers three algorithms for target motion analysis. The bounds indicate the criterion for target state observability, which can be summarised as a requirement for the observer to "outmanoeuvre" the target. The proposed algorithms for target motion analysis include the Maximum Likelihood estimator, the Extended Kalman filter (EKF) with and without angle parametrisation and the Regularised Particle filter. Considering both the statistical and computational performance of the proposed algorithms and based on extensive performance evaluation with simulated data, it appears that the angle-parametrised EKF is the preferred choice for implementation in an operational system.

The discussed algorithms for target motion analysis have been applied successfully to a set of real ISAR data (range profiles) collected in the recent trials with the Ingara radar. The results indicate that target motion analysis based on range and range-rate measurements can converge towards a steady state in less than three minutes for a typical scenario of interest.

Authors



Branko Ristic

Surveillance Systems Division

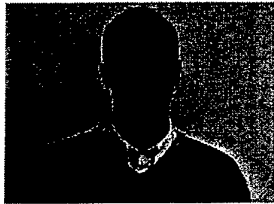
Branko Ristic received his first two degrees in Yugoslavia: BEng from the University of Novi Sad in 1984 and MSc from The Belgrade University in 1991 (both in Electrical Engineering). He received the PhD degree from the Signal Processing Research Centre at Queensland University of Technology (QUT) in 1995. Between 1984 and 1989 he was a research engineer in the Vinca Institute in Belgrade. In February 1989 he arrived to Australia and became a senior research assistant at The University of Queensland (1989-1991) and QUT (1991-1993), a senior DSP engineer in GEC Marconi Systems (1995) and a Research Fellow at QUT (1996). In May 1996 he joined DSTO where he was initially working on enhancements to the Jindalee radar tracker. He is currently a Senior Research Scientist responsible for algorithm development and performance analysis of tracking and multi-sensor integration systems on airborne platforms. His main research interests include estimation theory, target tracking and non-linear filtering.



Sanjeev Arulampalam

Surveillance Systems Division

Sanjeev Arulampalam received the B.Sc degree in Mathematical Sciences and the B.E degree with first class honours in Electrical and Electronic Engineering from the University of Adelaide in 1991 and 1992, respectively. In 1992 he joined the staff of Computer Sciences of Australia (CSA) where he worked as a Software Engineer in the Safety Critical Software Systems group. At CSA he was responsible for undertaking a hazard analysis on a computerised train control system. In 1993, he won a Telstra Postgraduate Fellowship award to work toward a Ph.D degree in Electrical and Electronic Engineering at the University of Melbourne, which he completed in 1997. Upon completion of his postgraduate studies, Dr Arulampalam joined DSTO in 1998 as a Research Scientist. Since then he has worked on tender evaluation of the AEW&C contracts and angle-only target motion analysis for the F/A-18 project. Currently he is on a long term attachment to DERA, Malvern where he is involved in research into the fusion of radar with IRST data. His research interests include estimation theory, signal processing, and target motion analysis.



James McCarthy

Surveillance Systems Division

James McCarthy received a B.E. (Hons.) degree in 1995 and a BSc in 1996 both from the University of Adelaide. He has been with the Surveillance Systems Division of the Defence Science and Technology Organisation (DSTO) since 1995. There he has worked in the area of maritime surveillance radar on ISAR signal processing and target classification, airborne radar system software design and the implementation of maritime surveillance radar modes.

Contents

Glossary	ix
1 Introduction	1
2 Problem description	2
2.1 Background	2
2.2 Mathematical formulation	3
3 Cramér-Rao Lower Bounds	5
3.1 Derivation of the Bounds	5
3.2 Analysis of the Bounds	8
3.3 Bounds with the use of prior knowledge	9
4 Tracking Algorithms	13
4.1 Maximum Likelihood Estimation	13
4.2 Angle-Parametrised Extended Kalman filter	13
4.2.1 Extended Kalman filter	13
4.2.2 Angle Parametrisation	14
4.3 Regularised Particle filter	16
4.3.1 SIR algorithm	16
4.3.2 Regularisation	17
5 Algorithm Performance and Comparison	18
5.1 Performance of the MLE	19
5.2 Performance of the EKF	20
5.3 Performance of the RPF	21
6 Application to Ingara ISAR Data	22
6.1 The ISAR mode of Ingara radar for data collection	22
6.2 Coordinate transformations	23
6.3 Pre-processing of the ISAR data	25
6.4 Range-only TMA from the ISAR data	25
7 Summary	27

References

28

Figures

1	<i>A typical range-only tracking scenario.</i>	2
2	<i>A tracking scenario used for the analysis of Cramér-Rao lower bounds</i>	8
3	<i>Cramér-Rao lower bounds: (a) position x_k (solid line) and y_k (dashed line); (b) velocity \dot{x}_k (solid line) and \dot{y}_k (dashed line)</i>	9
4	<i>Cramér-Rao lower bounds of the position estimates in x and y direction . . .</i>	10
5	<i>Comparison of square-rooted Cramér-Rao lower bounds (x position only) with and without the use of prior information</i>	12
6	<i>The statistical performance of the MLE against the CRLB: (a) x position and (b) y position</i>	19
7	<i>The statistical performance of the EKF against the CRLB (with prior knowl- edge of $\sigma_v = 10$ m/s): (a) x position and (b) y position. The dotted line is the MLE error curve.</i>	20
8	<i>The statistical performance of the AP-EKF against the CRLB (with prior knowledge of $\sigma_v = 10$ m/s): (a) x position and (b) y position. The dotted line is the MLE error curve.</i>	21
9	<i>The statistical performance of the RPF with $N = 2000, 5000$ and 10000 particles. The CRLBs (using prior knowledge of $\sigma_v = 10$ m/s) are shown with dashed lines; the EKF curves are plotted with dotted lines. (a) x position and (b) y position.</i>	22
10	<i>Coordinate systems.</i>	23
11	<i>The geographic location of the data collection scenario</i>	26
12	<i>Own-ship position and velocity in the local coordinates</i>	27
13	<i>Target range and range-rate measurements</i>	28
14	<i>The measured range and range-rate against what would have been measured, had the MLE estimated target state been correct</i>	29
15	<i>Estimated target trajectories: (a) local Cartesian coordinates; (b) geographic map; (c) AP-EKF with uncertainty ellipses (local coordinates)</i>	30

Tables

1	<i>Parameters used in Ingara ISAR mode</i>	23
---	--	----

Glossary

AP-EKF Angle parametrised Extended Kalman filter

CRLB Cramér-Rao lower bound

EKF Extended Kalman filter

FIM Fisher Information Matrix

MLE Maximum Likelihood estimator

ISAR Inverse Synthetic Aperture Radar

RPF Regularised particle filter

RMS Root-mean-square

1 Introduction

The problem of target tracking or target motion analysis (TMA) using range and range-rate measurements is motivated by its application to maritime surveillance with the Ingara Multi-Mode Radar [5]. In particular, one of the maritime surveillance modes of Ingara is the Inverse Synthetic Aperture Radar (ISAR) mode [7], in which the radar collects high-resolution range profiles of the target, processed in real-time to generate ISAR images. The problem, however, is that during the collection of the range-profiles, the antenna spotlights the location on the sea-surface where the target was initially detected, while in reality the target is moving and at some stage disappears from the radar antenna beam in azimuth or the sampled swath in range. Therefore there is a need to track the target in the ISAR mode using only the information contained in the ISAR range profiles. This information can be presented in the form of the target range and range-rate measurements for tracking. If target tracking is possible with these measurements, the output of the tracker could be used to automatically control the range gate setting and antenna pointing.

Tracking targets with range only measurements has attracted very little research interest in the past. To our best knowledge, the only publication devoted to this problem, [19], discusses the conditions for target observability from range-only measurements. It concludes that if the target is moving at a constant acceleration the observer must be moving with a non-zero jerk in order to observe the target. This condition appears to be identical to the observability criterion for the related and extensively studied problem of angle-only target motion analysis [10], [4, Ch.5].

This report makes three main contributions. First it derives the theoretical Cramér-Rao (CR) bounds of performance for the target tracking problem with range and range-rate measurements. The bounds, which define the best achievable performance, depend on the target-observer geometry, the accuracy of measurements and the sampling interval. The derivation assumes unity probability of detection and zero probability of false alarm (i.e. no uncertainty with respect to the origin of measurements) as well as non-maneuvring target motion. The bounds are derived for the recursive type estimators with prior information and automatically provide the criterion for observability. The second contribution of the report is the design of three algorithms for state estimation and their comparison with the derived CR bounds. The problem of range-only tracking is a non-linear problem, and the proposed algorithms include: (i) the Maximum likelihood estimator (MLE) over a cumulative measurement set; (ii) the Extended Kalman filter (EKF) with angle-parametrisation and (iii) the Regularised Particle filter (RPF). The MLE is a batch algorithm, but in this application it is applied to a set of measurements collected within a sliding time interval. Both the EKF and the RPF are recursive algorithms. The third contribution of the report is the application of the developed range-only tracking theory to a set of real ISAR data collected in the recent trials with the Ingara radar.

The report is organised as follows. Section 2 describes the motivation for range-only tracking in ISAR imaging and provides a mathematical formulation of the problem. The CR lower bounds of performance are derived and discussed in Section 3. Section 4 presents the three proposed tracking algorithms. Their statistical and computational performance is compared in Section 5. Section 6 is devoted to the application of the range-only TMA algorithms to a set of ISAR range-profiles collected by the Ingara radar. Section 7 sum-

marises the main results of the report.

2 Problem description

2.1 Background

Two of the maritime surveillance modes of the Ingara radar are the Scan mode [15] and the ISAR mode [7]. In typical wide area maritime surveillance, an airborne observer is using the radar Scan mode to detect and locate maritime surface vessels. Once the location of a target is known, the radar operator switches the radar into the ISAR mode to collect high resolution range profiles of the target. The range profiles are processed into the ISAR images and shown to the operator in real-time. In the ISAR mode, the radar antenna is controlled in such a manner that it “spotlights” the ocean surface at the target coordinates which were obtained from the initial detection in the radar Scan mode. If the target is moving, however, at some point of time it will move out of the radar antenna beam either in the cross-range direction or the sampled swath in the range direction. Because we wish to continuously collect the data in the ISAR mode, we would like to be able to track the target using only the information contained in the ISAR range profiles. This would enable the radar antenna beam to be steered always towards the target. The information contained in the high-resolution range profiles can be converted to the target range and range-rate measurements by linear regression of the target range centroids, applied over a sliding time window.

This motivates the theoretical consideration of the problem of target motion analysis or target tracking, using only the available measurements of target range and range-rate. Before developing the tracking algorithms the fundamental questions to be answered are: is the range tracking feasible (the observability criterion) and how fast the algorithms can converge. Note that for the ISAR data collection purposes, the observer is usually flying along a circular trajectory, as illustrated in Figure 1. This is the type of the observer trajectory we will consider in the report.

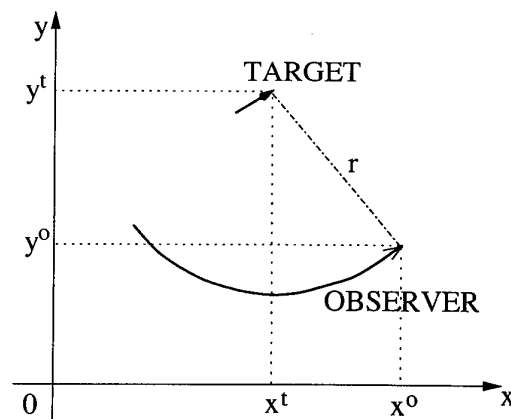


Figure 1: A typical range-only tracking scenario.

2.2 Mathematical formulation

The target is assumed to move at a constant velocity along a straight line in the x - y plane (Figure 1). Although in reality the target-observer scenario is three-dimensional, it suffices to define and study the problem in two dimensions, because the slant range and range-rate can be readily converted to the ground range and range-rate¹. For the typical ranges of interest the curvature of the Earth can be neglected and hence we assume the local tangential plane (flat Earth) model.

The basic problem is to estimate the target kinematic state (position, heading, speed) from noise corrupted measurements. The target kinematic state can be fully described by the state vector defined in the discrete-time as:

$$\mathbf{s}_k^t = [x_k^t \ \dot{x}_k^t \ y_k^t \ \dot{y}_k^t]^T \quad (1)$$

where T denotes matrix transpose, x_k^t and y_k^t are the Cartesian target coordinates at time index k and \dot{x}_k^t and \dot{y}_k^t are their respective derivatives (velocities). For the assumed target motion model, \dot{x}_k^t and \dot{y}_k^t are constant in time. Knowing the target state vector it is then straightforward to calculate the target heading or speed. The observer state, defined as

$$\mathbf{s}_k^o = [x_k^o \ \dot{x}_k^o \ y_k^o \ \dot{y}_k^o]^T \quad (2)$$

is assumed to be known (information supplied by an on-board Inertial Navigation System). The relative state vector is given by:

$$\mathbf{s}_k = \mathbf{s}_k^t - \mathbf{s}_k^o = [x_k \ \dot{x}_k \ y_k \ \dot{y}_k]^T. \quad (3)$$

The available measurements of target range and range-rate are available at time instants

$$t_k = t_0 + T_d + (k-1)T_s, \quad k = 1, 2, \dots \quad (4)$$

where T_s is the sampling interval in the ISAR mode and $T_d \gg T_s$ is the period of time required for the radar to switch from the Scan mode to the ISAR mode. The assumption is that the measurement origin is unambiguous² and that the target is detected with the probability 1. The measurement vector at time instants t_k is defined by:

$$\mathbf{z}_k = \begin{bmatrix} r_k \\ \dot{r}_k \end{bmatrix} \quad (k = 1, 2, \dots) \quad (5)$$

and the measurement equation is given by:

$$\mathbf{z}_k = \mathbf{h}'(\mathbf{s}_k) + \mathbf{w}_k \quad (6)$$

$$\begin{bmatrix} r_k \\ \dot{r}_k \end{bmatrix} = \begin{bmatrix} h_r(\mathbf{s}_k) \\ h_{\dot{r}}(\mathbf{s}_k) \end{bmatrix} + \mathbf{w}_k \quad (7)$$

¹The transformation from slant to ground range and range-rate is straightforward since the target is always on the surface of the Earth and the observer height is constant and known during the observation interval.

²Measurement origin ambiguity could be caused for example by multiple targets or possibly false measurements.

where

$$h_r(\mathbf{s}_k) = \sqrt{x_k^2 + y_k^2} \quad (8)$$

$$h_\theta(\mathbf{s}_k) = \frac{x_k \dot{x}_k + y_k \dot{y}_k}{\sqrt{x_k^2 + y_k^2}}. \quad (9)$$

The noise process \mathbf{w}_k in (6) is i.i.d. zero-mean Gaussian with covariance \mathbf{R} , that is $\mathbf{w}_k \sim \mathcal{N}(\mathbf{0}; \mathbf{R})$.

The information about the target state at time t_0 is available in form of the measurement of the target location (range and azimuth) provided by the radar in the Scan mode. This measurement is denoted by

$$\mathbf{z}_0 = \begin{bmatrix} r_0 \\ \theta_0 \end{bmatrix} \quad (10)$$

and the measurement equation at t_0 is given by:

$$\mathbf{z}_0 = \mathbf{h}''(\mathbf{s}_0) + \mathbf{w}_0 \quad (11)$$

$$\begin{bmatrix} r_0 \\ \theta_0 \end{bmatrix} = \begin{bmatrix} h_r(\mathbf{s}_0) \\ h_\theta(\mathbf{s}_0) \end{bmatrix} + \mathbf{w}_0 \quad (12)$$

where $h_r(\cdot)$ was defined by (8) and

$$h_\theta(\mathbf{s}_0) = \arctan\left(\frac{x_0}{y_0}\right). \quad (13)$$

In (13), x_0 and y_0 are the relative target Cartesian coordinates at $k = 0$ and can be worked out from the measurement at t_0 , \mathbf{z}_0 (which is in polar coordinates). Note that azimuth θ_0 is defined as the angle from the observer to the target, referenced clockwise positive to the y -axis. The noise process \mathbf{w}_0 in (11) is independent from \mathbf{w}_k , $k = 1, 2, \dots$ and distributed as $\mathbf{w}_0 \sim \mathcal{N}(\mathbf{0}; \mathbf{R}_0)$.

The state equation for this problem can be written as:

$$\mathbf{s}_{k+1} = \mathbf{F}_k \mathbf{s}_k - \mathbf{U}_{k+1,k} \quad (14)$$

where \mathbf{F}_k is the transition matrix defined as

$$\mathbf{F}_k = \begin{bmatrix} 1 & T_k & 0 & 0 \\ 0 & 1 & 0 & 0 \\ 0 & 0 & 1 & T_k \\ 0 & 0 & 0 & 1 \end{bmatrix}, \quad (15)$$

T_k is the sampling interval, given by

$$T_k = \begin{cases} T_d & k = 0 \\ T_s & k = 1, 2, \dots \end{cases} \quad (16)$$

and

$$\mathbf{U}_{k+1,k} = \begin{bmatrix} x_{k+1}^o - x_k^o - T_k \dot{x}_k^o \\ \dot{x}_{k+1}^o - \dot{x}_k^o \\ y_{k+1}^o - y_k^o - T_k \dot{y}_k^o \\ \dot{y}_{k+1}^o - \dot{y}_k^o \end{bmatrix}$$

is a vector of deterministic inputs which account for the observer acceleration. Note that the model of the state equation (14) is purely deterministic.

3 Cramér-Rao Lower Bounds

3.1 Derivation of the Bounds

The Cramér-Rao lower bound (CRLB) for an unbiased estimator $\hat{\mathbf{s}}_k^t$ of the target state vector at time t_k , is given by the inverse of the Fisher information matrix (FIM),

$$\mathbb{E} \left\{ (\hat{\mathbf{s}}_k^t - \mathbf{s}_k^t) (\hat{\mathbf{s}}_k^t - \mathbf{s}_k^t)^T \right\} \geq \mathbf{J}_k^{-1}, \quad (k = 1, 2, \dots). \quad (17)$$

Since the observer motion is deterministic, the same CRLB as in (17) applies to an unbiased estimator of the *relative* target state vector $\hat{\mathbf{s}}_k$. The FIM in (17) is defined as [20]:

$$\mathbf{J}_k = \mathbb{E} \left\{ [\nabla \lambda(\mathbf{s}_k^t)] [\nabla \lambda(\mathbf{s}_k^t)]^T \right\} \quad (18)$$

where $\lambda(\mathbf{s}_k^t)$ is the negative log-likelihood function

$$\lambda(\mathbf{s}_k^t) = -\log p(\mathbf{Z}_k | \mathbf{s}_k^t), \quad (19)$$

and ∇ is the gradient with respect to the target state vector \mathbf{s}_k^t . The term \mathbf{Z}_k in (19) represents the collection of all measurements up to time t_k , i.e. $\mathbf{Z}_k = \{\mathbf{z}_i\}_{i=0}^k$.

Due to the assumption we made about the independence of measurement noise, the likelihood function can be expressed by a product:

$$p(\mathbf{Z}_k | \mathbf{s}_k^t) = \prod_{i=0}^k p(\mathbf{z}_i | \mathbf{s}_k^t). \quad (20)$$

Furthermore, since the measurement noise is zero-mean Gaussian

$$p(\mathbf{z}_i | \mathbf{s}_k^t) = \begin{cases} \mathcal{N}(\mathbf{h}''[\mathbf{s}_0(\mathbf{s}_k^t)]; \mathbf{R}_0) & i = 0 \\ \mathcal{N}(\mathbf{h}'[\mathbf{s}_i(\mathbf{s}_k^t)]; \mathbf{R}) & i = 1, 2, \dots, k \end{cases} \quad (21)$$

$$= \begin{cases} \frac{1}{2\pi\sqrt{|\mathbf{R}_0|}} \exp \left[-\frac{1}{2}(\mathbf{z}_0 - \mathbf{h}''[\mathbf{s}_0(\mathbf{s}_k^t)])^T \mathbf{R}_0 (\mathbf{z}_0 - \mathbf{h}''[\mathbf{s}_0(\mathbf{s}_k^t)]) \right] & i = 0 \\ \frac{1}{2\pi\sqrt{|\mathbf{R}|}} \exp \left[-\frac{1}{2}(\mathbf{z}_i - \mathbf{h}'[\mathbf{s}_i(\mathbf{s}_k^t)])^T \mathbf{R} (\mathbf{z}_i - \mathbf{h}'[\mathbf{s}_i(\mathbf{s}_k^t)]) \right] & i = 1, 2, \dots, k. \end{cases} \quad (22)$$

Functions $\mathbf{h}'(\cdot)$ and $\mathbf{h}''(\cdot)$ in (22) were defined in Section 2.2 as

$$\mathbf{h}'(\cdot) = \begin{pmatrix} h_r(\cdot) \\ h_{\dot{r}}(\cdot) \end{pmatrix} \quad \text{and} \quad \mathbf{h}''(\cdot) = \begin{pmatrix} h_r(\cdot) \\ h_{\theta}(\cdot) \end{pmatrix} \quad (23)$$

with $h_r(\cdot)$, $h_{\dot{r}}(\cdot)$ and $h_{\theta}(\cdot)$ given by eqs.(8), (9) and (13) respectively. The crucial point here is to observe that the arguments of $\mathbf{h}'(\cdot)$ and $\mathbf{h}''(\cdot)$ have to be expressed as the respective functions of \mathbf{s}_k^t . This means that

1. x_0 and y_0 in (13) should be expressed as

$$x_0(\mathbf{s}_k^t) = x_k^t - (t_k - t_0)\dot{x}_k^t - x_0^o \quad (24)$$

$$y_0(\mathbf{s}_k^t) = y_k^t - (t_k - t_0)\dot{y}_k^t - y_0^o \quad (25)$$

which follows from the earlier assumption that $\dot{x}_k^t = \text{const}$ and $\dot{y}_k^t = \text{const}$. Note from (4) that $t_k - t_0 = T_d + (k-1)T_s$.

2. x_i , y_i , \dot{x}_i and \dot{y}_i ($i = 1, 2, \dots, k$) which according to (22) are to be used in eqs.(8) and (9) have to be expressed as:

$$x_i(\mathbf{s}_k^t) = x_k^t - (k-i) T_s \dot{x}_k^t - x_i^o \quad (26)$$

$$y_i(\mathbf{s}_k^t) = y_k^t - (k-i) T_s \dot{y}_k^t - y_i^o \quad (27)$$

$$\dot{x}_i(\mathbf{s}_k^t) = \dot{x}_k^t - \dot{x}_i^o \quad (28)$$

$$\dot{y}_i(\mathbf{s}_k^t) = \dot{y}_k^t - \dot{y}_i^o. \quad (29)$$

Again eqs.(26)-(29) follow from $\dot{x}_k^t = \text{const}$ and $\dot{y}_k^t = \text{const}$.

From (19) and (22) it follows that the log-likelihood function can be expressed as:

$$\begin{aligned} \lambda(\mathbf{s}_k^t) &= C + \frac{1}{2} \{ \mathbf{z}_0 - \mathbf{h}''[\mathbf{s}_0(\mathbf{s}_k^t)] \} \mathbf{R}_0^{-1} \{ \mathbf{z}_0 - \mathbf{h}''[\mathbf{s}_0(\mathbf{s}_k^t)] \}^T + \\ &\quad \frac{1}{2} \sum_{i=1}^k \{ \mathbf{z}_i - \mathbf{h}'[\mathbf{s}_i(\mathbf{s}_k^t)] \} \mathbf{R}^{-1} \{ \mathbf{z}_i - \mathbf{h}'[\mathbf{s}_i(\mathbf{s}_k^t)] \}^T \\ &= C + \lambda_0 + \sum_{i=1}^k \lambda_i \end{aligned} \quad (30)$$

where C is a constant. Next we need to find the gradient of the log-likelihood function λ expressed by (30), which using the basic rules of matrix algebra [12] yields:

$$\nabla \lambda(\mathbf{s}_k^t) = \nabla \lambda_0 + \sum_{i=1}^k \nabla \lambda_i \quad (31)$$

with

$$\nabla \lambda_0 = -\nabla[\mathbf{h}'']^T \mathbf{R}_0^{-1} [\mathbf{z}_0 - \mathbf{h}''] \quad (32)$$

$$\nabla \lambda_i = -\nabla[\mathbf{h}']^T \mathbf{R}^{-1} [\mathbf{z}_i - \mathbf{h}'] \quad (i = 1, 2, \dots, k) \quad (33)$$

The FIM of eq.(17) is then

$$\mathbf{J}_k = \mathbf{E} \left\{ \left[\sum_{i=0}^k \nabla \lambda_i \right] \left[\sum_{i=0}^k \nabla \lambda_i \right]^T \right\} \quad (34)$$

which due to the mutual independence of measurements leads to

$$\mathbf{J}_k = [\nabla[\mathbf{h}'']^T] \mathbf{R}_0^{-1} [\nabla[\mathbf{h}'']^T]^T + \sum_{i=1}^k [\nabla[\mathbf{h}']^T] \mathbf{R}^{-1} [\nabla[\mathbf{h}']^T]^T \quad (35)$$

It remains to find the analytic expressions for

$$\nabla[\mathbf{h}']^T = \begin{bmatrix} \frac{\partial h_r[\mathbf{s}_i(\mathbf{s}_k^t)]}{\partial x_k^t} & \frac{\partial h_r[\mathbf{s}_i(\mathbf{s}_k^t)]}{\partial x_k^t} \\ \frac{\partial h_r[\mathbf{s}_i(\mathbf{s}_k^t)]}{\partial \dot{x}_k^t} & \frac{\partial h_r[\mathbf{s}_i(\mathbf{s}_k^t)]}{\partial \dot{x}_k^t} \\ \frac{\partial h_r[\mathbf{s}_i(\mathbf{s}_k^t)]}{\partial y_k^t} & \frac{\partial h_r[\mathbf{s}_i(\mathbf{s}_k^t)]}{\partial y_k^t} \\ \frac{\partial h_r[\mathbf{s}_i(\mathbf{s}_k^t)]}{\partial \dot{y}_k^t} & \frac{\partial h_r[\mathbf{s}_i(\mathbf{s}_k^t)]}{\partial \dot{y}_k^t} \end{bmatrix} \quad \text{and} \quad \nabla[\mathbf{h}'']^T = \begin{bmatrix} \frac{\partial h_r[\mathbf{s}_0(\mathbf{s}_k^t)]}{\partial x_k^t} & \frac{\partial h_\theta[\mathbf{s}_0(\mathbf{s}_k^t)]}{\partial x_k^t} \\ \frac{\partial h_r[\mathbf{s}_0(\mathbf{s}_k^t)]}{\partial \dot{x}_k^t} & \frac{\partial h_\theta[\mathbf{s}_0(\mathbf{s}_k^t)]}{\partial \dot{x}_k^t} \\ \frac{\partial h_r[\mathbf{s}_0(\mathbf{s}_k^t)]}{\partial y_k^t} & \frac{\partial h_\theta[\mathbf{s}_0(\mathbf{s}_k^t)]}{\partial y_k^t} \\ \frac{\partial h_r[\mathbf{s}_0(\mathbf{s}_k^t)]}{\partial \dot{y}_k^t} & \frac{\partial h_\theta[\mathbf{s}_0(\mathbf{s}_k^t)]}{\partial \dot{y}_k^t} \end{bmatrix}. \quad (36)$$

Using the differentiation rules, the unknown terms in (36) can be shown to be:

$$\frac{\partial h_r[\mathbf{s}_i(\mathbf{s}_k^t)]}{\partial x_k^t} = \frac{x_i}{\sqrt{x_i^2 + y_i^2}} \quad (37)$$

$$\frac{\partial h_r[\mathbf{s}_i(\mathbf{s}_k^t)]}{\partial \dot{x}_k^t} = -(k-i)T_s \frac{\partial h_r[\mathbf{s}_i(\mathbf{s}_k^t)]}{\partial x_k^t} \quad (38)$$

$$\frac{\partial h_r[\mathbf{s}_i(\mathbf{s}_k^t)]}{\partial y_k^t} = \frac{y_i}{\sqrt{x_i^2 + y_i^2}} \quad (39)$$

$$\frac{\partial h_r[\mathbf{s}_i(\mathbf{s}_k^t)]}{\partial \dot{y}_k^t} = -(k-i)T_s \frac{\partial h_r[\mathbf{s}_i(\mathbf{s}_k^t)]}{\partial y_k^t} \quad (40)$$

$$\frac{\partial h_r[\mathbf{s}_i(\mathbf{s}_k^t)]}{\partial x_k^t} = \frac{\dot{x}_i \sqrt{x_i^2 + y_i^2} - (x_i \dot{x}_i + y_i \dot{y}_i) \frac{x_i}{\sqrt{x_i^2 + y_i^2}}}{x_i^2 + y_i^2} \quad (41)$$

$$\frac{\partial h_r[\mathbf{s}_i(\mathbf{s}_k^t)]}{\partial \dot{x}_k^t} = \frac{[x_i - (k-i)T_s \dot{x}_i] \sqrt{x_i^2 + y_i^2} + (x_i \dot{x}_i + y_i \dot{y}_i) \frac{(k-i)T_s x_i}{\sqrt{x_i^2 + y_i^2}}}{x_i^2 + y_i^2} \quad (42)$$

$$\frac{\partial h_r[\mathbf{s}_i(\mathbf{s}_k^t)]}{\partial y_k^t} = \frac{\dot{y}_i \sqrt{x_i^2 + y_i^2} - (x_i \dot{x}_i + y_i \dot{y}_i) \frac{y_i}{\sqrt{x_i^2 + y_i^2}}}{x_i^2 + y_i^2} \quad (43)$$

$$\frac{\partial h_r[\mathbf{s}_i(\mathbf{s}_k^t)]}{\partial \dot{y}_k^t} = \frac{[y_i - (k-i)T_s \dot{y}_i] \sqrt{x_i^2 + y_i^2} + (x_i \dot{x}_i + y_i \dot{y}_i) \frac{(k-i)T_s y_i}{\sqrt{x_i^2 + y_i^2}}}{x_i^2 + y_i^2} \quad (44)$$

$$\frac{\partial h_r[\mathbf{s}_0(\mathbf{s}_k^t)]}{\partial x_k^t} = \frac{x_0}{\sqrt{x_0^2 + y_0^2}} \quad (45)$$

$$\frac{\partial h_r[\mathbf{s}_0(\mathbf{s}_k^t)]}{\partial \dot{x}_k^t} = -[(k-1)T_s + T_d] \frac{\partial h_r[\mathbf{s}_0(\mathbf{s}_k^t)]}{\partial x_k^t} \quad (46)$$

$$\frac{\partial h_r[\mathbf{s}_0(\mathbf{s}_k^t)]}{\partial y_k^t} = \frac{y_0}{\sqrt{x_0^2 + y_0^2}} \quad (47)$$

$$\frac{\partial h_r[\mathbf{s}_0(\mathbf{s}_k^t)]}{\partial \dot{y}_k^t} = -[(k-1)T_s + T_d] \frac{\partial h_r[\mathbf{s}_0(\mathbf{s}_k^t)]}{\partial y_k^t} \quad (48)$$

$$\frac{\partial h_\theta[\mathbf{s}_0(\mathbf{s}_k^t)]}{\partial x_k^t} = \frac{y_0}{x_0^2 + y_0^2} \quad (49)$$

$$\frac{\partial h_\theta[\mathbf{s}_0(\mathbf{s}_k^t)]}{\partial \dot{x}_k^t} = -[(k-1)T_s + T_d] \frac{\partial h_\theta[\mathbf{s}_0(\mathbf{s}_k^t)]}{\partial x_k^t} \quad (50)$$

$$\frac{\partial h_\theta[\mathbf{s}_0(\mathbf{s}_k^t)]}{\partial y_k^t} = -\frac{x_0}{x_0^2 + y_0^2} \quad (51)$$

$$\frac{\partial h_\theta[\mathbf{s}_0(\mathbf{s}_k^t)]}{\partial \dot{y}_k^t} = -[(k-1)T_s + T_d] \frac{\partial h_\theta[\mathbf{s}_0(\mathbf{s}_k^t)]}{\partial y_k^t} \quad (52)$$

The FIM given by (34) depends on: (i) the geometry of the considered scenario (target and observer trajectories); (ii) measurements accuracy (defined by the covariance matrices \mathbf{R}_0 and \mathbf{R}); (iii) time delay T_d and the sampling interval T_s . The CRLBs of the state vector

s_k^t are calculated as the diagonal elements of the inverse of the FIM, i.e.

$$\text{CRLB}\{[s_k^t]_j\} = [\mathbf{J}_k^{-1}]_{jj} \quad (j = 1, 2, 3, 4), \quad (53)$$

where $[s_k^t]_j$ refers to the j -th component of vector s_k^t . Note that the target observability implies that the FIM has an inverse matrix.

3.2 Analysis of the Bounds

Consider a scenario shown in Figure 2. The target is moving towards the north-east with a speed of 8 m/s. The observer is flying at a speed of 150 m/s along a circular path with a radius of approximately 15 km. At time t_0 , the observer is at a location with coordinates (50km, 35km) in Figure 2. The covariances are assumed to be $\mathbf{R}_0 = \text{diag}[400m^2, (3^\circ)^2]$ and $\mathbf{R} = \text{diag}[400m^2, 4m^2/s^2]$, with a time delay of $T_d = 40s$ and sampling interval $T_s = 1s$. The CRLB's (square-rooted) of unbiased estimators \hat{x}_k, \hat{y}_k ,

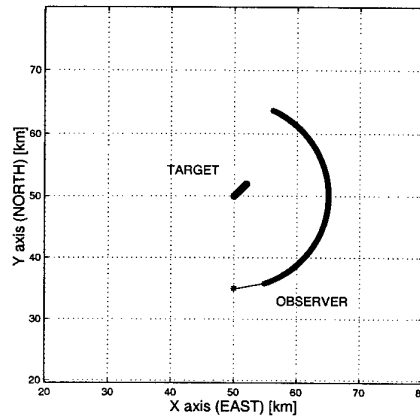


Figure 2: A tracking scenario used for the analysis of Cramér-Rao lower bounds

\hat{x}_k and \hat{y}_k ($k = 1, 2, \dots$), are shown in Figure 3 (starting from time instant $t_1 = t_0 + T_d$). Note that the initial range estimate is fairly accurate while the initial angular estimate is fairly poor. This translates in this particular observer-target scenario, into a more accurate initial estimate of the target position in y than along the x axis. With estimates of velocities \dot{x} and \dot{y} the situation is opposite.

Next we analyse the effect of the following parameters on the CRLBs: the time delay between the radar modes (T_d), the sampling interval (T_s), the radius of the observer circular path ρ and the standard deviation of the range-rate measurements $\sigma_{\dot{r}} = \sqrt{[\mathbf{R}]_{2,2}}$. The results are shown in Figure 4 for the same scenario and the parameters used in Figures 2 and 3, except for those parameters whose effect on the CRLBs is being analysed.

Somewhat surprisingly, the CRLBs in Figure 4.(a) and (b) suggest that longer radar mode switch delays, T_d , speed up the convergence of the range-only tracking. The explanation is that by extending T_d we effectively increase the duration of the total observation period $t_k - t_0$, which facilitates the state estimation.

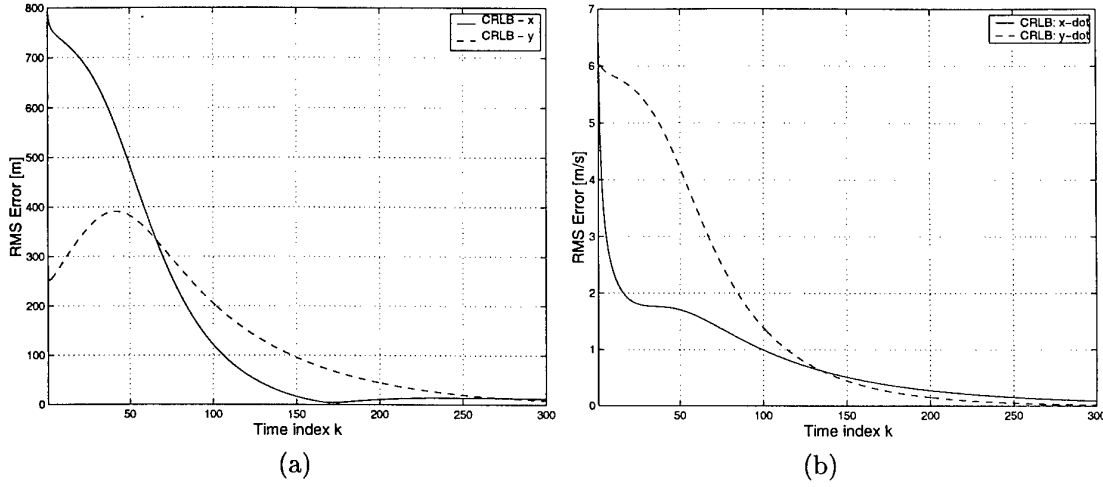


Figure 3: Cramér-Rao lower bounds: (a) position x_k (solid line) and y_k (dashed line); (b) velocity \dot{x}_k (solid line) and \dot{y}_k (dashed line)

By reducing the sampling interval, the total number of measurements is increased, and the estimates of the target position in the x and y directions are expected to be better, as confirmed by the CRLBs in Figure 4.(c) and (d). Note that this would increase the computational load of the algorithms.

The effect of varying the radius of the circular observer path, ρ , is shown in Figure 4.(e) and (f). Since the target is moving with a constant velocity along a straight line, the observability criterion [19] requires the observer to have a non-zero acceleration. The smaller the radius of the observer circular path, the larger the component of the observer acceleration, and consequently the faster the convergence of the state estimates from range and range-rate only measurements. It has been verified that if the observer is moving along a straight line with a constant velocity (same as the target), the CRLBs are monotonically increasing, thus confirming the observability requirement for non-zero acceleration.

The significance of the range-rate measurements, \dot{r}_k , is investigated in Figure 4.(g) and (h). Two cases are considered, the first with totally imprecise range-rate measurements (i.e. very large $[\mathbf{R}]_{2,2}$, mimicking the absence of \dot{r}_k) and the second with precise range-rate measurements $\sigma_{\dot{r}} = 1$ m/s. The CR bounds indicate that by using the precise range-rate measurements, the algorithm convergence can be improved. Since the algorithm convergence is of crucial importance in the application of interest, the range-rate measurements will be used for target tracking.

3.3 Bounds with the use of prior knowledge

The recursive Bayesian estimators, such as the Extended Kalman filter or the particle filter (described in depth in Section 4), in addition to all available measurements, \mathbf{Z}_k , make use of *prior knowledge* about the target motion for tracking. For the problem considered in this report, this could be prior knowledge of the maximum target speed.

The recursive Bayesian estimators typically estimate the relative target state vector

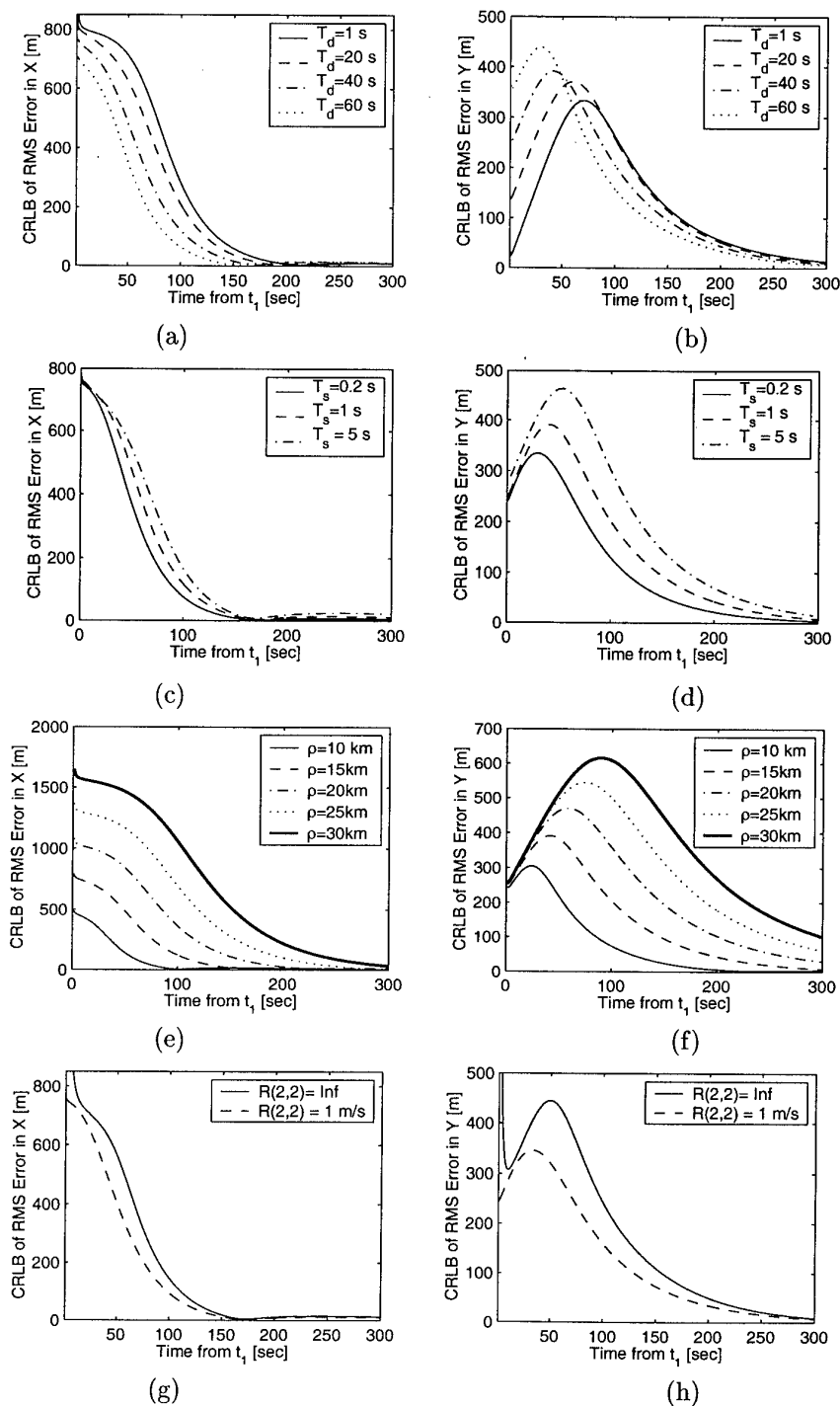


Figure 4: Cramér-Rao lower bounds of the position estimates in x and y direction, shown as a function of: T_d in (a) and (b); T_s in (c) and (d); ρ in (e) and (f); σ_r in (g) and (h)

and initialise the target track using the first measurement and the prior knowledge. For the problem considered in this report the initial measurement at t_0 , $\mathbf{z}_0 = [r_0, \theta_0]^T$, is in polar coordinates. The initial target state and its covariance are calculated by conversion from the polar to the Cartesian coordinates³, assuming that the covariance matrix \mathbf{R}_0 is diagonal with elements $\sigma_r = \sqrt{[\mathbf{R}_0]_{1,1}}$ and $\sigma_\theta = \sqrt{[\mathbf{R}_0]_{2,2}}$. The initial state vector is then

$$\hat{\mathbf{s}}_{0|0} = [r_0 \sin \theta_0 \quad -\dot{x}_0^o \quad r_0 \cos \theta_0 \quad -\dot{y}_0^o]^T \quad (54)$$

where \dot{x}_0^o and \dot{y}_0^o are the initial observer velocity components defined in eq.(2). The covariance matrix of the initial estimate is given by

$$\mathbf{P}_{0|0} = \begin{bmatrix} P_{11} & 0 & P_{13} & 0 \\ 0 & P_{22} & 0 & 0 \\ P_{31} & 0 & P_{33} & 0 \\ 0 & 0 & 0 & P_{44} \end{bmatrix}. \quad (55)$$

Note the initial target velocity components in (54) are set to zero, while their variance is given by the elements P_{22} and P_{44} of $\mathbf{P}_{0|0}$ in (55), i.e.

$$P_{22} = P_{44} = \sigma_v^2. \quad (56)$$

The remaining elements of $\mathbf{P}_{0|0}$ are as follows [8, p.155]:

$$\begin{aligned} P_{11} &= r_0^2 \sigma_\theta^2 \cos^2 \theta_0 + \sigma_r^2 \sin^2 \theta_0 \\ P_{33} &= r_0^2 \sigma_\theta^2 \sin^2 \theta_0 + \sigma_r^2 \cos^2 \theta_0 \\ P_{13} &= P_{31} = (\sigma_r^2 - r_0^2 \sigma_\theta^2) \sin \theta_0 \cos \theta_0. \end{aligned}$$

The prior target density at t_0 is assumed to be Gaussian, that is $\mathbf{s}_0 \sim \mathcal{N}(\hat{\mathbf{s}}_{0|0}, \mathbf{P}_{0|0})$. The contribution of this prior density now has to be worked out at the time index k . Due to the purely deterministic target motion, the following relationship holds:

$$\mathbf{s}_k = \mathbf{F}^k \mathbf{s}_0$$

where

$$\mathbf{F}^k = \begin{bmatrix} 1 & (k-1)T_s + T_d & 0 & 0 \\ 0 & 1 & 0 & 0 \\ 0 & 0 & 1 & (k-1)T_s + T_d \\ 0 & 0 & 0 & 1 \end{bmatrix}. \quad (57)$$

Then it follows (see for instance [13, Theorem 2.11]) that

$$\mathbf{s}_k \sim \mathcal{N}(\mathbf{F}^k \hat{\mathbf{s}}_{0|0}, \mathbf{F}^k \mathbf{P}_{0|0} [\mathbf{F}^k]^T).$$

The FIM at time index k for the recursive Bayesian estimators can be expressed as [20, pg.84] :

$$\mathbf{J}_k = \mathbf{J}_k^P + \mathbf{J}_k^M \quad (58)$$

³The so called "debiased consistent" conversion [14] is recommended for large values of σ_θ .

where [20, pg.85]

$$\mathbf{J}_k^P = [\mathbf{F}^k \mathbf{P}_{0|0} [\mathbf{F}^k]^T]^{-1} \quad (59)$$

is due to the initial measurement and the prior knowledge. The component of the FIM due to measurements, \mathbf{J}_k^M , follows from (35):

$$\mathbf{J}_k^M = \sum_{i=1}^k [\nabla[\mathbf{h}^i]^T] \mathbf{R}^{-1} [\nabla[\mathbf{h}^i]^T]^T. \quad (60)$$

Figure 5 compares the CRLB with and without the use of prior knowledge (x position only). The trajectories, measurement covariances, sampling interval and the initial delay are the same as for the CRLBs shown in Figure 3. The CRLBs in Figure 5 are shown for values of the standard deviation of velocity (σ_v in eq.(56)) of 5 m/s, 10 m/s and 20 m/s. Observe from Figure 5 that the CRLB which uses prior knowledge is initially lower,

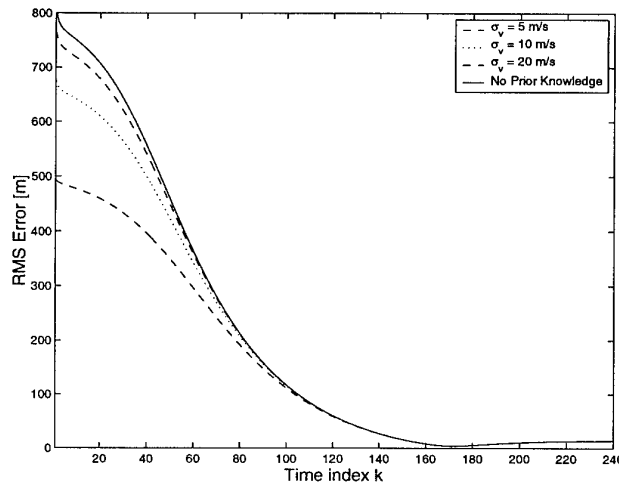


Figure 5: Comparison of square-rooted Cramér-Rao lower bounds (x position only) with and without the use of prior information

although the significance of prior information diminishes over time and the bounds become identical for $k > 100$. The quality of prior information is measured by its variance. Note that by increasing the value of σ_v (i.e. by reducing the quality of prior information), the CRLB with prior knowledge approaches the one with no prior knowledge. In summary, for large values of σ_v , the CRLB calculated using the FIM of eq.(35) and the CRLB calculated using the FIM of eq.(58) become identical. Note that the practical value of σ_v for range-only tracking of surface vessels is $\sigma_v \approx 10$ m/s (dotted line in Figure 5) where prior knowledge makes a measurable impact on the initial performance.

4 Tracking Algorithms

4.1 Maximum Likelihood Estimation

The Maximum Likelihood Estimator (MLE) [20] of the target state vector $\mathbf{s}_k^t = [x_k^t, y_k^t, \dot{y}_k^t]^T$ at time t_k is defined as the vector \mathbf{s}_k^t that maximises the likelihood function $p(\mathbf{Z}_k | \mathbf{s}_k^t)$, given by eqs.(20). This is equivalent to minimisation of the negative log-likelihood function $\lambda(\mathbf{s}_k^t)$, given by (30). The implementation is easier with the latter approach, hence we find the MLE as

$$\hat{\mathbf{s}}_{k,\text{MLE}}^t = \arg \min_{\mathbf{s}_k^t} \lambda(\mathbf{s}_k^t). \quad (61)$$

Minimisation is, in general, performed by numerical methods [18]. Our implementation is based on the MATLAB[®] built-in routine *fmins*. Note that the MLE is a batch algorithm - it operates on the accumulated set of all previous measurements. For on-line data processing applications (such as the one considered in this report), the MLE can be applied over a sliding window of accumulated measurements. From the theory it is known [20] that the MLE is an efficient estimator, and hence its variance should meet the theoretical CR lower bound derived in Section 3.1 (no use of prior knowledge).

4.2 Angle-Parametrised Extended Kalman filter

4.2.1 Extended Kalman filter

Target motion analysis using range and range-rate measurements only, is a non-linear dynamic state estimation problem because the measurement equation (6) is non-linear. The linear filtering algorithms such as the Kalman filter are therefore inappropriate, and the conventional approach is to approximate eq.(6) by a series expansion and then to use an equivalent measurement matrix in the ordinary Kalman filter equations. Such an estimator, known as the Extended Kalman filter (EKF) [2], is developed for the range-only tracking problem, with the first order series expansion (linearisation) of the non-linear measurement equation.

The recursive equations of the EKF are presented below. They describe how to evaluate the relative state estimate $\hat{\mathbf{s}}_{k+1|k+1}$ at t_{k+1} and its covariance matrix $\mathbf{P}_{k+1|k+1}$, given the measurement \mathbf{z}_{k+1} , and the estimate of the relative state vector \mathbf{s}_k at t_k , with its covariance matrix $\mathbf{P}_{k|k}$. The state prediction equation follows from (14):

$$\hat{\mathbf{s}}_{k+1|k} = \mathbf{F}_k \hat{\mathbf{s}}_{k|k} - \mathbf{U}_{k+1,k} \quad (62)$$

while the covariance prediction is given by

$$\mathbf{P}_{k+1|k} = \mathbf{F}_k \mathbf{P}_{k|k} \mathbf{F}_k^T.$$

The measurement prediction is given by:

$$\hat{\mathbf{z}}_{k+1|k} = \begin{bmatrix} \hat{r}_{k+1|k} \\ \hat{\dot{r}}_{k+1|k} \end{bmatrix} = \mathbf{h}'(\hat{\mathbf{s}}_{k+1|k})$$

with

$$\hat{r}_{k+1|k} = \sqrt{x_{k+1|k}^2 + y_{k+1|k}^2}, \quad (63)$$

$$\hat{r}_{k+1|k} = \frac{\hat{x}_{k+1|k}\hat{x}_{k+1|k} + \hat{y}_{k+1|k}\hat{y}_{k+1|k}}{\hat{r}_{k+1|k}}. \quad (64)$$

The Kalman gain matrix can be evaluated as:

$$\mathbf{W}_{k+1} = \mathbf{P}_{k+1|k} \mathbf{H}_{k+1}^T [\mathbf{H}_{k+1} \mathbf{P}_{k+1|k} \mathbf{H}_{k+1}^T + \mathbf{R}]^{-1}, \quad (65)$$

where \mathbf{R} is the covariance matrix of measurement noise in eq.(6), and \mathbf{H}_{k+1} is the linearised measurement matrix, evaluated at the predicted state, defined by:

$$[\mathbf{H}_{k+1}]_{ij} = \left. \frac{\partial [\mathbf{h}]_i}{\partial [\mathbf{s}]_j} \right|_{\mathbf{s}=\hat{\mathbf{s}}_{k+1|k}} = \begin{bmatrix} h_{11} & h_{12} & h_{13} & h_{14} \\ h_{21} & h_{22} & h_{23} & h_{24} \end{bmatrix}. \quad (66)$$

The elements of the matrix in (66) can be easily computed by differentiation:

$$h_{11} = \frac{\hat{x}_{k+1|k}}{\hat{r}_{k+1|k}}, \quad h_{12} = 0, \quad h_{13} = \frac{\hat{y}_{k+1|k}}{\hat{r}_{k+1|k}}, \quad h_{14} = 0 \quad (67)$$

$$\begin{aligned} h_{21} &= \frac{\hat{r}_{k+1|k}\hat{x}_{k+1|k} - \hat{x}_{k+1|k}\hat{r}_{k+1|k}}{\hat{r}_{k+1|k}^2}, \\ h_{22} &= h_{11} \\ h_{23} &= \frac{\hat{r}_{k+1|k}\hat{y}_{k+1|k} - \hat{y}_{k+1|k}\hat{r}_{k+1|k}}{\hat{r}_{k+1|k}^2}, \\ h_{24} &= h_{13}. \end{aligned} \quad (68)$$

The updated state and its covariance matrix are given by

$$\hat{\mathbf{s}}_{k+1|k+1} = \hat{\mathbf{s}}_{k+1|k} + \mathbf{W}_{k+1}[\mathbf{z}_{k+1} - \hat{\mathbf{z}}_{k+1|k}] \quad (69)$$

$$\mathbf{P}_{k+1|k+1} = [\mathbf{I} - \mathbf{W}_{k+1}\mathbf{H}_{k+1}]\mathbf{P}_{k+1|k} \quad (70)$$

where \mathbf{I} is the 4×4 identity matrix.

4.2.2 Angle Parametrisation

If the initial azimuth measurement is characterised by a fairly large variance, the convergence of the range-only TMA with an EKF can be improved by running in parallel a set of weighted EKFs, each with a different initial azimuth value. This type of a filter in the report will be referred to as the angle-parametrised EKF (AP-EKF). The idea used in the development of the AP-EKF closely resembles that of the range-parametrised EKF for angle-only tracking [17], [1].

Recall that the initial azimuth measurement is θ_0 with standard deviation σ_θ . We wish to construct N_f Extended Kalman filters, each with an initial angular accuracy N_f times

better than that of a single EKF. First define an interval in the angle domain with the limits $\theta_{\min} = \theta_0 - 3\sigma_\theta$ and $\theta_{\max} = \theta_0 + 3\sigma_\theta$. The interval is divided into N_f subintervals of width $\Delta\theta = (\theta_{\max} - \theta_{\min})/N_f$. The initial azimuth angle for EKF i is chosen to correspond the mid-point of the interval i , i.e.

$$\theta_i = \theta_{\min} + (i - 0.5) \Delta\theta, \quad i = 1, \dots, N_f,$$

with the standard deviation set to $\sigma_{\theta_i} = \sigma_\theta/N_f$.

The next step is to calculate the weights associated with each EKF at time t_{k+1} . This can be done recursively using Bayes' rule as:

$$w_{k+1}^i = \frac{p(\mathbf{z}_{k+1}|i) w_k^i}{\sum_{j=1}^{N_f} p(\mathbf{z}_{k+1}|j) w_k^j} \quad (71)$$

where $p(\mathbf{z}_{k+1}|i)$ is the likelihood of measurement \mathbf{z}_{k+1} , given that the i -th EKF is the correct one. Assuming Gaussian statistics, the likelihood $p(\mathbf{z}_{k+1}|i)$ can be computed as:

$$p(\mathbf{z}_{k+1}|i) = \frac{1}{2\pi|\mathbf{S}_{k+1}^i|^{\frac{1}{2}}} \exp \left\{ -\frac{1}{2} \left(\mathbf{z}_{k+1} - \hat{\mathbf{z}}_{k+1|k}^i \right)^T (\mathbf{S}_{k+1}^i)^{-1} \left(\mathbf{z}_{k+1} - \hat{\mathbf{z}}_{k+1|k}^i \right) \right\} \quad (72)$$

where $\hat{\mathbf{z}}_{k+1|k}^i$ is the predicted measurement vector at $k+1$ for EKF i and \mathbf{S}_{k+1}^i is the innovation covariance for EKF i , given by:

$$\mathbf{S}_{k+1}^i = \mathbf{H}_{k+1} \mathbf{P}_{k+1|k}^i \mathbf{H}_{k+1}^T + \mathbf{R}. \quad (73)$$

In (73), \mathbf{H}_{k+1} is the linearised measurement vector defined by eqs.(66)-(68), $\mathbf{P}_{k+1|k}^i$ is the covariance matrix of the predicted state of the i -th filter.

The initial weights w_0^i are computed assuming that the true initial azimuth obeys a Gaussian distribution with mean θ_0 and variance σ_θ^2 , i.e.

$$w_0^i = \frac{1}{\sqrt{2\pi}\sigma_\theta} \int_{\theta_L^i}^{\theta_R^i} e^{-\frac{(\theta - \theta_0)^2}{2\sigma_\theta^2}} d\theta \quad (74)$$

where $\theta_L^i = \theta_{\min} + (i-1)\Delta\theta$ and $\theta_R^i = \theta_L^i + \Delta\theta$ are the lower and upper limits of the i -th subinterval, respectively.

Suppose the updated state estimate of EKF i at t_k is denoted by $\hat{\mathbf{s}}_{k|k}^i$. The combined AP-EKF state vector and its covariance are calculated using the Gaussian mixture formulae [2, p.47]:

$$\hat{\mathbf{s}}_{k|k} = \sum_{i=1}^{N_f} w_k^i \hat{\mathbf{s}}_{k|k}^i \quad (75)$$

$$\mathbf{P}_{k|k} = \sum_{i=1}^{N_f} w_k^i \left[\mathbf{P}_{k|k}^i + (\hat{\mathbf{s}}_{k|k}^i - \hat{\mathbf{s}}_{k|k})(\hat{\mathbf{s}}_{k|k}^i - \hat{\mathbf{s}}_{k|k})' \right]. \quad (76)$$

The improved tracking performance of the AP-EKF tracker is achieved by using N_f independent trackers, each with a much smaller initial angular measurement variance than

that of a single EKF. This improvement is achieved at the expense of an N_f -fold increase in the computational load if all the angle subintervals are processed throughout. However, it has been found that generally the weighting of some of the subintervals rapidly reduces to zero. In such cases, the corresponding filters can be removed from the tracking process without loss of accuracy, thereby reducing the processing requirement. Thus, a weighting threshold can be set and any filter corresponding to a subinterval with a weight less than the threshold may be removed from the tracking process.

4.3 Regularised Particle filter

The particle filter (PF) is a technique for implementing a recursive Bayesian filter by Monte-Carlo simulations [6]. The optimum recursive Bayesian filter in the *Minimum Mean Square Error* (MMSE) sense is the mean of the posterior density [13]. The key idea of the PF is to represent the required posterior density function by a set of random samples or “particles”, and to compute the state estimate based on these samples. As the number of samples becomes very large, this Monte-Carlo characterisation becomes an equivalent representation to the usual functional description of the posterior pdf, and the particle filter estimate approaches the optimal Bayesian estimate.

4.3.1 SIR algorithm

In order to recursively compute the state estimates with the PF, the Monte Carlo representation of $p(\mathbf{s}_k|\mathbf{Z}_k)$ has to be *propagated in time*. The original particle (a.k.a. bootstrap) filter, proposed by Gordon et al. [11], was using the Sampling Importance Resampling (SIR) algorithm to propagate and update the particles. Assume at time t_{k-1} we have a set of independent and identically distributed (i.i.d) random samples $\{\mathbf{s}_{k-1}^i\}_{i=1}^N$ from the posterior pdf $p(\mathbf{s}_{k-1}|\mathbf{Z}_{k-1})$. Then for large N this pdf can be approximated as:

$$p(\mathbf{s}_{k-1}|\mathbf{Z}_{k-1}) \approx \sum_{i=1}^N \delta(\mathbf{s}_{k-1} - \mathbf{s}_{k-1}^i), \quad (77)$$

where $\delta(\cdot)$ is the Dirac delta function. The SIR algorithm propagates the random sample $\{\mathbf{s}_{k-1}^i\}_{i=1}^N$ drawn from $p(\mathbf{s}_{k-1}|\mathbf{Z}_{k-1})$, to a new random sample $\{\mathbf{s}_k^i\}_{i=1}^N$ which is approximately distributed according to $p(\mathbf{s}_k|\mathbf{Z}_k)$. This is performed as follows. According to the Bayes rule the posterior pdf at k can be written as [13, Sec.6.6]:

$$p(\mathbf{s}_k|\mathbf{Z}_k) \propto p(\mathbf{z}_k|\mathbf{s}_k) p(\mathbf{s}_k|\mathbf{Z}_{k-1}) \quad (78)$$

where the prediction density $p(\mathbf{s}_k|\mathbf{Z}_{k-1})$ is accomplished via

$$p(\mathbf{s}_k|\mathbf{Z}^{k-1}) = \int p(\mathbf{s}_k|\mathbf{s}_{k-1}) p(\mathbf{s}_{k-1}|\mathbf{Z}_{k-1}) d\mathbf{s}_{k-1}. \quad (79)$$

Using (77) in (79), the prediction density can be approximated as

$$p(\mathbf{s}_k|\mathbf{Z}^{k-1}) \approx \frac{1}{N} \sum_{i=1}^N p(\mathbf{s}_k|\mathbf{s}_{k-1}^i). \quad (80)$$

The sample from $p(\mathbf{s}_k|\mathbf{Z}_k)$ is generated in two stages, namely prediction and update. In the prediction stage, N random samples are generated from the prediction density $p(\mathbf{s}_k|\mathbf{Z}_{k-1})$ given in (80). This is done by passing the sample $\{\mathbf{s}_{k-1}^i\}_{i=1}^N$ through the state dynamic model of eq.(14). Note that in the absence of process noise in the state dynamics (the case we are considering in this report) the propagation of particles is purely deterministic. The resulting random sample $\{\mathbf{s}_k^{*i}\}_{i=1}^N$ is approximately distributed according to $p(\mathbf{s}_k|\mathbf{Z}^{k-1})$. In the update stage, the new sample $\{\mathbf{s}_k^i\}_{i=1}^N$ is generated by resampling N times from an approximate discrete representation of $p(\mathbf{s}_k|\mathbf{Z}_k)$ given by:

$$p(\mathbf{s}_k|\mathbf{Z}_k) \approx \sum_{i=1}^N q_k^i \delta(\mathbf{s}_k - \mathbf{s}_k^{*i}) \quad (81)$$

where

$$q_k^i = \frac{p(\mathbf{z}_k|\mathbf{s}_k^{*i})}{\sum_{j=1}^N p(\mathbf{z}_k|\mathbf{s}_k^{*j})}. \quad (82)$$

In other words, samples $\{\mathbf{s}_k^i\}_{i=1}^N$ are generated from the discrete set $\{\mathbf{s}_k^{*i}\}_{i=1}^N$ such that $Pr(\mathbf{s}_k^i = \mathbf{s}_k^{*i}) = q_k^i$. Note that in the update stage, the measurement \mathbf{z}_k is used to evaluate the likelihood functions $p(\mathbf{z}_k|\mathbf{s}_k^{*i})$ in (82).

A common problem, particularly prevalent in dynamical systems with small or zero process noise, is the sample impoverishment phenomenon, where the number of distinct particles at each time step monotonically decreases. If the problem is not addressed properly, it will lead to “particle collapse”, where all N particles occupy the same point in the state space, giving a poor representation of the posterior density.

4.3.2 Regularisation

An effective scheme that overcomes the sample impoverishment problem is known as the regularisation of the particle filter [16]. The resulting filter, the Regularised Particle filter (RPF), differs from the SIR in the resampling step only. The RPF resamples from a continuous approximation of the posterior density $p(\mathbf{s}_k|\mathbf{Z}_k)$, while the SIR resamples from the discrete approximation (81). Specifically, in the RPF, samples are drawn from the approximation:

$$p(\mathbf{s}_k|\mathbf{Z}_k) \approx \sum_{i=1}^N q_k^i K_h(\mathbf{s}_k - \mathbf{s}_k^{*i}) \quad (83)$$

where

$$K_h(\mathbf{s}) = \frac{1}{h^{n_s}} K\left(\frac{\mathbf{s}}{h}\right) \quad (84)$$

is the re-scaled kernel density $K(\cdot)$, $h > 0$ is the kernel bandwidth (a scalar parameter), and n_s is the dimension of the state vector \mathbf{s} . The kernel density is a symmetric probability density function such that

$$\int \mathbf{s} K(\mathbf{s}) d\mathbf{s} = 0, \quad \int \|\mathbf{s}\|^2 K(\mathbf{s}) d\mathbf{s} < \infty. \quad (85)$$

The kernel $K(\cdot)$ and bandwidth h are chosen so as to minimise the mean integrated square error between the true posterior density and the corresponding regularised empirical representation in (83). In the special case of an equally weighted sample, i.e. with $q_k^i = 1/N$ for $i = 1, 2, \dots, N$, the optimal choice of the kernel is the Epanechnikov kernel [16],

$$K_{\text{opt}} = \begin{cases} \frac{n_s+2}{2c_{n_s}}(1 - \|\mathbf{s}\|^2) & \text{if } \|\mathbf{s}\| < 1 \\ 0 & \text{otherwise.} \end{cases} \quad (86)$$

When the underlying density is Gaussian with a unit covariance matrix, the optimal choice for the bandwidth is

$$h_{\text{opt}} = A(k) N^{-\frac{1}{n_s+4}} \quad (87)$$

$$A(k) = [8c_{n_s}^{-1}(n_s+4)(2\sqrt{\pi})^{n_s}]^{\frac{1}{n_s+4}} \quad (88)$$

where c_{n_s} is the volume of the unit hypersphere in \mathbb{R}^{n_s} . The general formula for c_{n_s} is given in [3, p.96]. For the state vector as in (3), $n_s = 4$ and $c_4 = \pi^2/2$.

The implementation of the RPF is described next. The prediction step is the same as in the SIR algorithm, and it creates a random sample $\{\mathbf{s}_k^{*i}\}_{i=1}^N$. Now instead of resampling directly from $\{\mathbf{s}_k^{*i}\}_{i=1}^N$ as done by SIR, the following algorithm is implemented:

1. Draw N indices $\{l_i\}_{i=1}^N$ from a set $\{1, \dots, N\}$ so that $Pr\{l_i = j\} = q_k^j$, where $j = 1, \dots, N$.
2. Calculate the empirical covariance matrix \mathbf{S}_k^* of $\{\mathbf{s}_k^{*l_i}\}_{i=1}^N$.
3. For each $i = 1, \dots, N$
 - a. Generate a random variable $\epsilon^i \sim K$ from Epanechnikov kernel.
 - b. Compute

$$\mathbf{s}_k^i = \mathbf{s}_k^{*l_i} + h_{\text{opt}} \mathbf{D}_k \epsilon^i \quad (89)$$

where \mathbf{D}_k is the square root of the empirical covariance matrix \mathbf{S}_k^* , i.e. $\mathbf{D}_k \mathbf{D}_k^T = \mathbf{S}_k^*$.

By following this procedure we generate a random sample $\{\mathbf{s}_k^i\}_{i=1}^N$ drawn from (83).

5 Algorithm Performance and Comparison

The statistical performance of the TMA algorithms is analysed by Monte Carlo simulations. The trajectories, the measurement covariances \mathbf{R} and \mathbf{R}_0 , the sampling interval T_s and the initial delay T_d have the same values as described in Section 3.2. The resulting error curves are compared to the theoretically derived Cramér-Rao lower bounds.

Define the estimation error as:

$$\mathbf{e}_k = \hat{\mathbf{s}}_{k|k}^t - \mathbf{s}_k^t. \quad (90)$$

The performance of the TMA algorithms is measured by the root mean square (RMS) error. For component j of the state vector, the RMS error is defined as

$$\sigma_{[e_k]_j} = \sqrt{E \{ [e_k]_j - E\{[\hat{e}_k]_j\} \}^2} \quad (91)$$

and approximated with M Monte Carlo runs as follows:

$$\hat{\sigma}_{[e_k]_j} \approx \sqrt{\frac{1}{M} \sum_{k=1}^M \left\{ [\hat{e}_k]_j - \frac{1}{M} \sum_{k=1}^M [\hat{e}_k]_j \right\}^2} \quad (92)$$

The theoretical CR bound is derived earlier for unbiased estimators. Its square root represents the lower bound for RMS error of any unbiased TMA algorithm, i.e.

$$\sigma_{[e_k]_j} \geq \sqrt{\text{CRLB}\{[s_k^t]_j\}} \quad (93)$$

where $\text{CRLB}\{[s_k^t]_j\}$ is given by eq.(53). In all simulation results we used $M = 100$ independent Monte Carlo runs.

5.1 Performance of the MLE

The statistical performance of the Maximum likelihood estimator is shown in Figure 6 (x and y position only, i.e. $j = 1, 3$ in (92)). Since the MLE is not a Bayesian estimator, its performance is compared to the CRLB with no use of prior knowledge. Figure 6 confirms the theoretical assertion that the MLE for range-only TMA is an efficient estimator: it has no bias and its RMS error attains the square-root of the calculated CRLB.

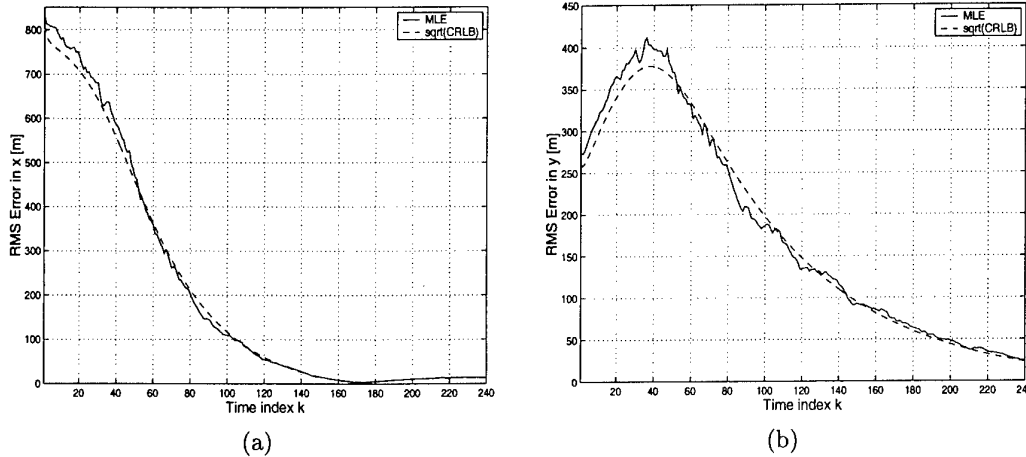


Figure 6: The statistical performance of the MLE against the CRLB: (a) x position and (b) y position

The main disadvantage of the MLE is its computational complexity. Not only is the numerical minimisation of the log-likelihood function in (61) a computationally demanding operation, but also at every time index k the MLE must operate on the accumulated set of

all previous measurements⁴ \mathbf{Z}_k . Using the same scenario as before, we compared the CPU time required by the MLE algorithm to that of the EKF algorithm. Both algorithms were implemented in MATLAB[®], and the comparison is performed at time index $k = 240$. It appears that the MLE requires 580 times more CPU time than the EKF.

5.2 Performance of the EKF

The statistical performance of the EKF based range-only TMA algorithm is shown in Figure 7 (x and y position only, i.e. $j = 1, 3$ in (92)). The EKF is a Bayesian estimator, hence its performance is compared to the CRLB with the prior knowledge of $\sigma_v = 10$ m/s. For comparison sake, the MLE performance curves are indicated by a dotted line.

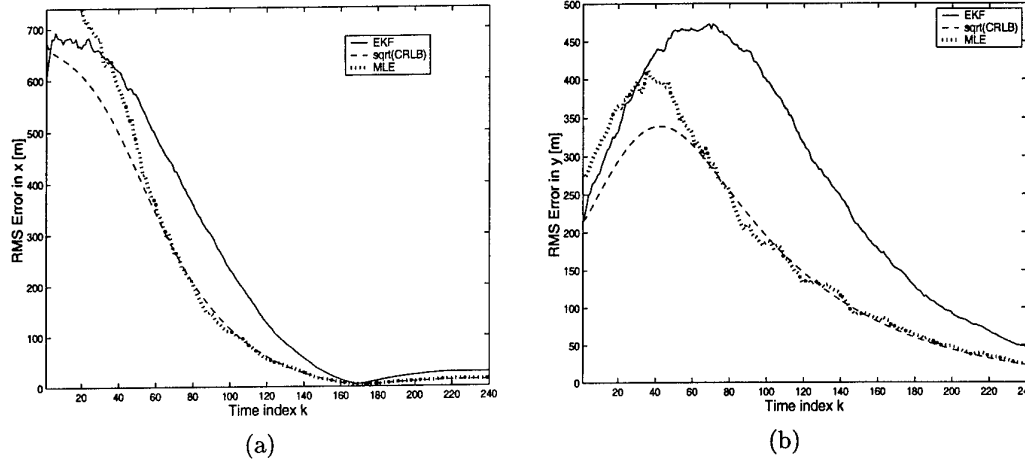


Figure 7: The statistical performance of the EKF against the CRLB (with prior knowledge of $\sigma_v = 10$ m/s): (a) x position and (b) y position. The dotted line is the MLE error curve.

Observe from Figure 7 that the EKF error is initially smaller than the MLE error, since the EKF uses the prior knowledge about the maximum target velocity. As the time progresses, however, the EKF quickly departs from the CRLB, and in general demonstrates a slower convergence than the MLE. This is particularly pronounced in Figure 7.(b). The suboptimal performance of the EKF is due to the approximation (linearisation) of the non-linear measurement equation.

Angle parametrisation described in Section 4.2.2 effectively resolves this problem. The results, obtained using $N_f = 5$ EKF filters, are shown in Figure 8. Again, the performance of the AP-EKF is compared to the CRLB with the prior knowledge of $\sigma_v = 10$ m/s, and the MLE error curves are indicated by a dotted line for comparison. Initially, the AP-EKF outperforms the MLE (by using the prior knowledge of the maximum target velocity), and subsequently its performance is very close to that of the MLE. Overall, this represents a huge improvement over the EKF. Our implementation of the AP-EKF (in the worst case) required $N_f = 5$ times more CPU time than the EKF and $580/N_f = 116$ times less CPU time than the MLE.

⁴By restricting the MLE to operate on the sliding window of previous measurements, the efficiency of the MLE is lost.

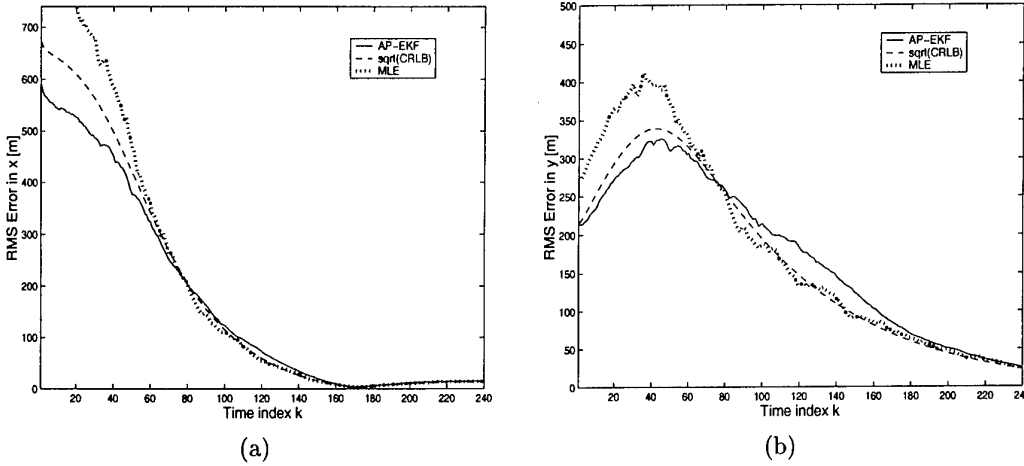


Figure 8: The statistical performance of the AP-EKF against the CRLB (with prior knowledge of $\sigma_v = 10$ m/s): (a) x position and (b) y position. The dotted line is the MLE error curve.

It should be emphasised that in all simulations the value of $\sigma_\theta = \sqrt{[\mathbf{R}_0]_{22}} = 3^\circ$ was used. However, if the accuracy of the initial angular measurement is higher (i.e. $\sigma_\theta < 1^\circ$), the EKF based TMA actually attains its corresponding CRLB and the angle parametrisation of the EKF is unnecessary.

5.3 Performance of the RPF

The Regularised Particle filter was included for consideration in this study of range-only TMA algorithms, mainly because it approaches in theory (with large number of particles N) the optimal recursive Bayesian estimator for what is essentially a non-linear dynamic estimation problem.

In order to be fair, the RPF should be compared to the EKF filter for range-only TMA, because the angle parametrisation technique discussed above in the context of EKF is equally applicable to the RPF. Figure 9 shows the statistical error performance of the RPF based TMA algorithm (x and y positions only) with $N = 2000, 5000$ and 10000 particles. For comparison sake, the CRLBs (using the prior knowledge of $\sigma_v = 10$ m/s) and the EKF error curves are shown as well. Observe that as the number of particles N is increased, the performance of the RPF improves, and in the limit approaches the CRLBs. This improvement, however, is at the expense of a corresponding increase in the computational load of the RPF. Thus the RPF with 2000, 5000 and 10000 particles requires 30, 70 and 134 times more CPU time respectively, than the EKF. Note also that at the end of the observation period, the RMS error of the EKF is slightly better than the RMS error of the RPF. This is due to the sample impoverishment in the particle filter, which has an effect towards the end of the observation period despite regularisation.

Finally, we make an overall comment with respect to the performance of various range-only TMA algorithms. It appears that the AP-EKF would be the strongest candidate for the considered application. The AP-EKF combines the satisfactory statistical performance, robustness to the initial measurement accuracy and the speed of execution. An-

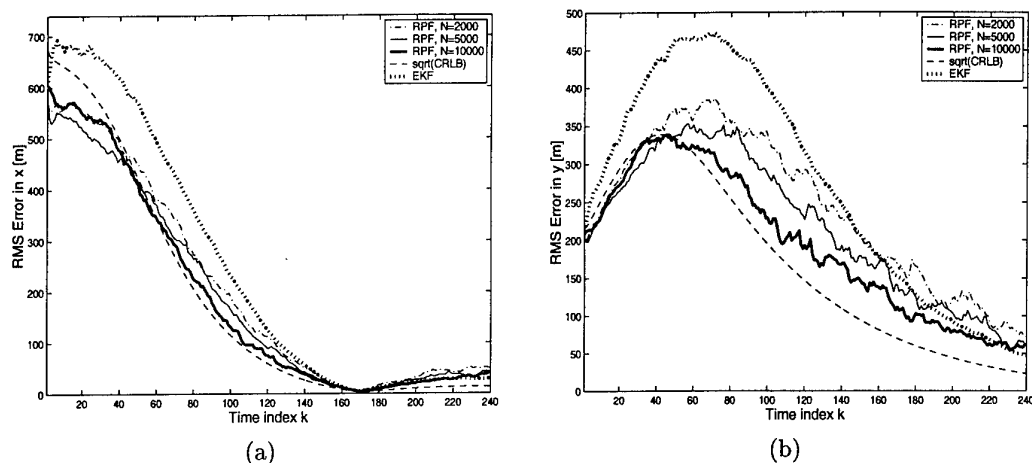


Figure 9: The statistical performance of the RPF with $N = 2000$, 5000 and 10000 particles. The CRLBs (using prior knowledge of $\sigma_v = 10$ m/s) are shown with dashed lines; the EKF curves are plotted with dotted lines. (a) x position and (b) y position.

other advantage of the AP-EKF over the MLE is that it can directly incorporate a small level of process noise in the dynamic equation (14). This can be important for modelling small changes in the target velocity resulting from the rough sea in windy conditions.

6 Application to Ingara ISAR Data

6.1 The ISAR mode of Ingara radar for data collection

Inverse Synthetic Aperture Radar (ISAR) is a technique for generating high-resolution radar images in range and Doppler (cross-range). This is achieved by sampling radar echoes from a target and coherently processing blocks of echoes to form ISAR images. The high resolution in range is achieved by using a stretch waveform while the high resolution in cross-range is achieved by processing a large aperture of data. A comprehensive treatment of ISAR theory is given in [21].

The ISAR mode on Ingara has been developed by Surveillance Systems Division of DSTO. A series of trials have been conducted to build up a database of ISAR imagery of a representative collection of target types to assist in the process of operator training and for further research into automatic target recognition. The ISAR mode of the Ingara radar collects and coherently processes high resolution range profiles into ISAR images for real-time display. This is achieved by “spotlighting” a maritime surface vessel during the data collection. The typical radar parameters used for the ISAR mode are shown in Table 1.

The application of range-only tracking algorithms to a set of real ISAR data will be described below. The Ingara radar is installed on a Beechcraft KingAir 350 aircraft, and targets of opportunity were used in data collection.

Table 1: Parameters used in Ingara ISAR mode

Radar Parameters	
A/D sampling rate	100 MHz
RF Bandwidth	400 MHz
Pulse Width	18 μ s
Number of samples	2048
Slant range resolution	0.33 m
Typical target range	20 km
PRF	600 Hz
Transmitted power	5 kW
Polarisation	VV

But first, we review the coordinate conversion techniques, necessary for transformation of radar measurements to the local tangential plane Cartesian coordinate system, which was assumed from Section 2 to Section 5.

6.2 Coordinate transformations

Four coordinate systems are used in the analysis of ISAR real data (Fig.10). The own-ship coordinates, supplied by the on-board global positioning system (GPS), are given in the *geodetic* coordinate system. The TMA problem and the corresponding algorithms (Sections 2-5) are defined in the *tangential-plane Cartesian* coordinate system. The radar measurements (range, range-rate, initial azimuth) are collected in the *local polar* coordinates. Finally the transformation between the geodetic and the tangential-plane Cartesian coordinate systems is done via *Earth-Centered Earth-Fixed (ECEF)* coordinates. The conversions between the coordinates is described below following [9, Chap.2]. Note however that the conversion from the local polar to the local Cartesian coordinates is not necessary as the TMA algorithms use the radar measurements directly.

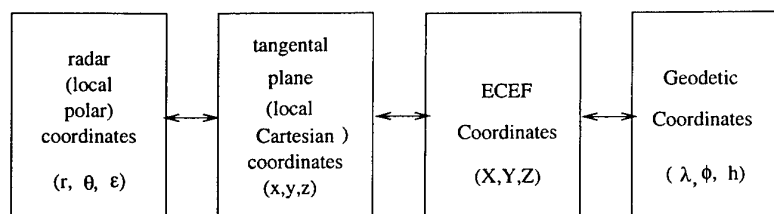


Figure 10: Coordinate systems.

Geodetic to ECEF and vice versa. In the geodetic coordinate system, a point on the ellipsoidal earth is represented by a triple (λ, ϕ, h) , where λ is latitude, ϕ is longitude and h is the altitude above the reference ellipsoid. In the ECEF rectangular coordinates (X, Y, Z) , the origin is in the center of the earth. The X axis extends through the inter-

section of the prime (0° longitude) meridian and the equator (0° latitude). The Z axis extends through the north pole (coincides with the earth's spin axis). The Y axis completes the right-handed coordinate system, passing through the equator and 90° longitude. The earth geoid is approximated by an ellipsoid of revolution about its minor axis. The parameters of the chosen approximating ellipsoid must be defined for a geodetic system, and in our case this is the WGS-84 ellipsoid. Its defining parameters are the semimajor and semiminor axis lengths a and b respectively [9, p.26]. The coordinate transformations from geodetic to ECEF coordinates are as follows:

$$\begin{aligned} X &= (N + h) \cos \lambda \cos \phi \\ Y &= (N + h) \cos \lambda \sin \phi \end{aligned} \quad (94)$$

$$Z = [N(1 - e^2) + h] \sin \lambda \quad (95)$$

where e is the eccentricity of the ellipsoid (for WGS-84, $e = 0.0818$) and

$$N(\lambda) = \frac{a}{\sqrt{1 - e^2 \sin^2 \lambda}}. \quad (96)$$

The conversion from the ECEF to the geodetic coordinates is more complicated and we used the iterative solution described in [9, p.28].

ECEF to tangent-plane and vice versa. The local tangent-plane coordinate system is the east-north-up rectangular coordinate system we often refer to in our everyday life. It is determined by the fitting of a tangent plane to the surface of the earth at some convenient (reference) point for local measurements (typically in vicinity of the data collection scenario). This reference point is the origin of the local frame. The x axis points to true east; the y axis points north and the z axis completes the right-handed coordinate system pointing up. For a moving own-ship, the tangent-plane origin is fixed.

The transformation matrix for transformation from ECEF to tangent-plane representation is given by [9, p.35]:

$$\mathcal{L} = \begin{bmatrix} -\sin \phi & \cos \phi & 0 \\ -\sin \lambda \cos \phi & -\sin \lambda \sin \phi & \cos \lambda \\ \cos \lambda \cos \phi & \cos \lambda \sin \phi & \sin \lambda \end{bmatrix}. \quad (97)$$

If the coordinates of the reference point in ECEF are (X_0, Y_0, Z_0) , then the transformation from an ECEF point (X, Y, Z) to the local tangent-plane coordinates (x, y, z) is as follows:

$$\begin{bmatrix} x \\ y \\ z \end{bmatrix} = \mathcal{L} \left(\begin{bmatrix} X \\ Y \\ Z \end{bmatrix} - \begin{bmatrix} X_0 \\ Y_0 \\ Z_0 \end{bmatrix} \right). \quad (98)$$

The inverse transformation is then:

$$\begin{bmatrix} X \\ Y \\ Z \end{bmatrix} = \begin{bmatrix} X_0 \\ Y_0 \\ Z_0 \end{bmatrix} + \mathcal{L}^T \begin{bmatrix} x \\ y \\ z \end{bmatrix}. \quad (99)$$

6.3 Pre-processing of the ISAR data

The target measurements which feed the TMA algorithms are obtained by pre-processing a large number of range profiles as follows. The data is divided into contiguous blocks corresponding to the desired update rate for the tracker. The estimates of target range and range-rate (referred to earlier as measurements r_k and \dot{r}_k) are computed for each block. In this particular case we adopt the sampling rate of 1 Hz (i.e. $T_s = 1$ s) and since the radar PRF is 600 Hz, a block size of 600 range profiles is used to compute each pair r_k and \dot{r}_k . An initial range estimate is formed by averaging the first few range profiles at the start of the very first block and by computing its "centroid" (a weighted mean). This is only done for the first block and represents the nominal target range at the start of the ISAR data. Each subsequent range profile (from the second onwards) is correlated with the first profile and the correlation lag (the shift in the position of the maximum in the correlation sequence) is due to target motion. Only shifts of ± 1 range bin from one profile to the next are allowed because the target cannot physically move faster. Any shift of more than ± 1 bin is replaced by a zero shift because this indicates bad or missing data in that profile (e.g. due to interference or hardware fault). Having computed the target shift for each profile by correlation, we fit through them a line by the least-squares method. The range-rate \dot{r}_k is calculated by taking the slope of that line. The target range from the middle profile of the block is used as the range estimate r_k . For each subsequent block the same procedure is repeated, except that the initial range estimate of the block is not formed by the centroid of the averaged range profiles, but simply by using the range estimate from the last range profile of the previous block.

With the described procedure for calculation of r_k and \dot{r}_k , the assumptions made in relation to the measurement noise \mathbf{w}_k in (6), become satisfied in a broad sense. In addition, the measurements of range r_k and range-rate \dot{r}_k are uncorrelated (i.e. the covariance matrix \mathbf{R} is diagonal).

6.4 Range-only TMA from the ISAR data

The geographic location of the data collection scenario is shown in Figure 11. The initial observer position and the initial target location measurement are indicated by \diamond and \star respectively. The reference point (the origin of the local coordinates) is shown as \square . The observer trajectory after the time delay of $T_d = 65$ sec is plotted by a solid line. The sampling interval (i.e. the time increment of the sliding window used for pre-processing range profiles) is $T_s = 1$ sec. The observer height was constant at 210 m.

The own-ship position and velocity, computed from the supplied INS/GPS data and transformed into the local tangent plane, are shown in Figure 12. Finally the range and the range rate measurements are displayed in Figure 13. Occasional outliers in the measurements are filtered out using a median filter of windowlength 3. Since the target range is approximately 20 km (see Figure 13.a), in all our TMA calculations we neglect the own-ship height, and assume that the observer and the target are co-planar. The error in the measured range due to this approximation is less than 1 m.

The ISAR data were collected using the targets of opportunity. While the true target state over the observation period is unknown, we have two means of testing and verifying

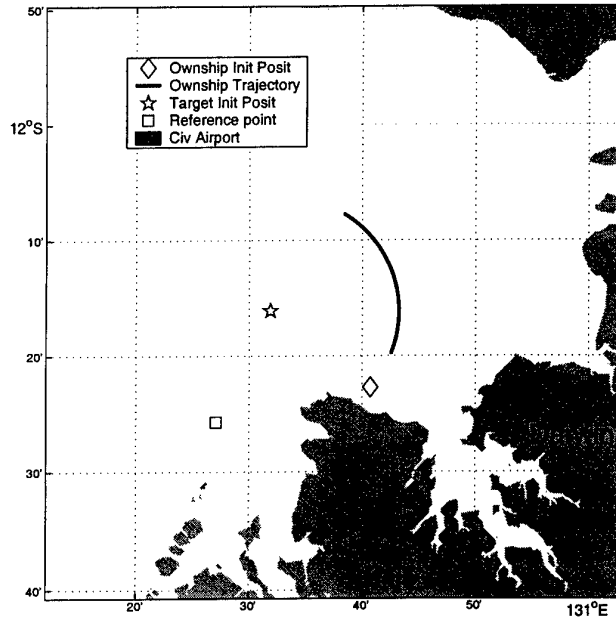


Figure 11: The geographic location of the data collection scenario

the TMA algorithm performance.

First we apply the MLE TMA algorithm on the entire measurement set \mathbf{Z}_K , (where K is the total number of available measurements) and then compare the measured range and range-rate with what would have been measured, had the estimated target state been correct. The result of this test with $\mathbf{R} = \text{diag}[(20\text{m})^2; (3\text{m/s})^2]$ and $\mathbf{R}_0 = \text{diag}[(20\text{m})^2; (1^\circ)^2]$ is shown in Figure 14. We note in the range plot (Figure 14.a) that the two curves appear to be identical, except at $t_0 = 0$, where the discrepancy is about 200 m. This is due to the lack of own-ship motion compensation during the period of time T_d required for the radar mode switching (the own-ship data were unavailable during this interval). The range-rate curves in Figure 14.b are also very close, well within the assumed standard deviation of the range-rate error of $\sqrt{[\mathbf{R}]_{22}} = 3 \text{ m/s}$. This result gives us confidence that the MLE estimate taken using the entire measurement set \mathbf{Z}_K is accurate.

The second test uses the information about the true target heading, which was measured independently as 287° clockwise positive with respect to North. Assuming the target position measurement at t_0 (that is \mathbf{z}_0) is exact and using the estimate of the target speed (5.9 m/s) obtained from the MLE state estimate, we obtain what we refer to as the incomplete truth data about the target. The target trajectory based on incomplete truth is shown in Figure 15 by a dotted line. For comparison, Figure 15.a further displays the estimated target trajectories of the progressive MLE (applied to \mathbf{Z}_k , $k = 1, \dots, K$); the angle-parametrised EKF and the Regularised PF. The AP-EKF was using $N_f = 5$ filters and both AP-EKF and RPF used $\sigma_v = 10 \text{ m/s}$. Note that all three algorithms fairly accurately follow the indicated target heading. The MLE and the AP-EKF converge towards the true trajectory after approximately 2.5 minutes, while the RPF convergence is somewhat slower. For completeness, Figure 15.b displays the MLE estimated target trajectory

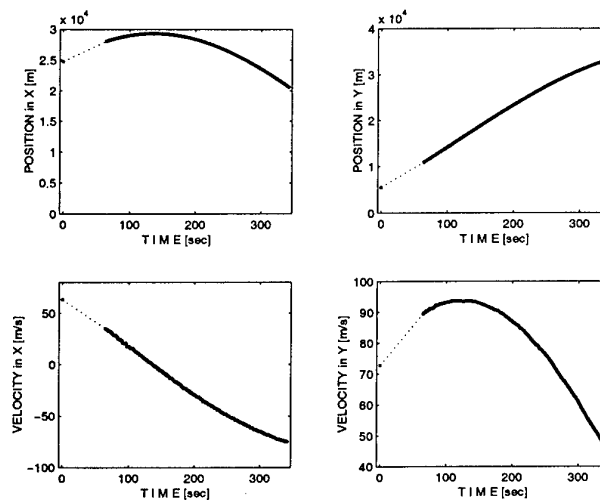


Figure 12: Own-ship position and velocity in the local coordinates

on a geographic map (in geodetic coordinates). Finally Figure 15.c repeats the estimated target trajectory obtained with the AP-EKF, but it incorporates the 2-sigma uncertainty ellipses. Note that these ellipses: (i) always include the true target position; (ii) reduce in size as time progresses; (iii) indicate a large uncertainty in angle (not measured) but small in range; (iv) have a long axes always orthogonal to the “line-of-sight”.

7 Summary

The report describes an investigation of the problem of target motion analysis from range and range-rate measurements. The problem is of importance for tracking surface vessels while collecting data in the ISAR mode of the Ingara multi-mode radar. The report derived the bounds of performance and considered three algorithms for target motion analysis. The proposed algorithms include the Maximum Likelihood estimator, the Extended Kalman filter with and without angle parametrisation and the Regularised Particle filter. Considering both the statistical and computational performance of the proposed algorithms, this study recommends the angle-parametrised EKF as the preferred choice for implementation in an operational system.

The discussed TMA algorithms have been applied successfully to one set of real ISAR data collected in the recent trials with the Ingara radar. The results indicate that target motion analysis based on range and range-rate measurements can converge towards a steady state in less than three minutes for a typical scenario of interest for ISAR data collection.

Future work would involve real-time implementation of the recommended range-only tracking algorithm on Ingara system.

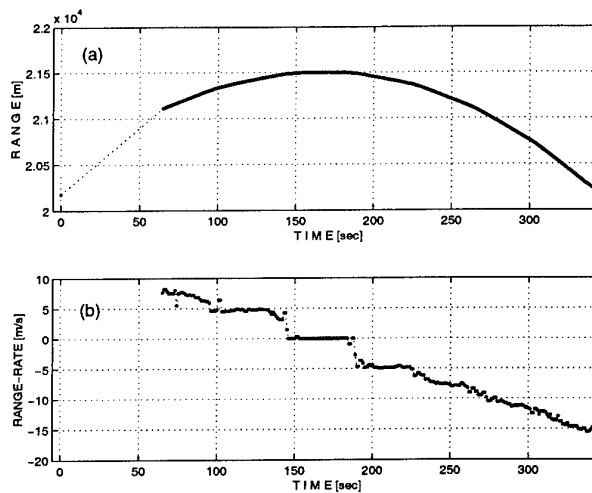


Figure 13: Target range and range-rate measurements

References

1. S. Arulampalam and B. Ristic. Comparison of the particle filter with range-parametrised and modified polar EKF's for angle-only tracking. In *Proc. of SPIE*, volume 4048, pages 288–299, 2000.
2. Y. Bar-Shalom and X. R. Li. *Estimation and Tracking*. Artech House, 1993.
3. Y. Bar-Shalom and X. R. Li. *Multitarget-Multisensor Tracking*. YBS, 1995.
4. S. Blackman and R. Popoli. *Design and Analysis of Modern Tracking Systems*. Artech House, 1999.
5. I. Bostock. Ingara radar demonstrated by army. *Jane's international defense review*, 33(8):8, Aug. 2000.
6. A. Doucet, N. deFreitas, and N. J. Gordon, editors. *Sequential Monte Carlo Methods in Practice*. Springer-Verlag, New York, 2001.
7. C. Fantarella. A real-time ISAR mode for the Ingara multi-mode radar. Technical Report DSTO-TR-1036, Defence Science and Technology Organisation, Salisbury, Australia, October 2000.
8. A. Farina and F. A. Studer. *Radar Data Processing*. John Wiley, 1985.
9. J. Farrell and M. Barth. *The Global Positioning System and Inertial Navigation*. McGraw-Hill, 1998.
10. E. Fogel and M. Gavish. Nth-order dynamics target observability from angle measurements. *IEEE Trans. Aerospace and Electronic Systems*, AES-24(3):305–308, May 1988.

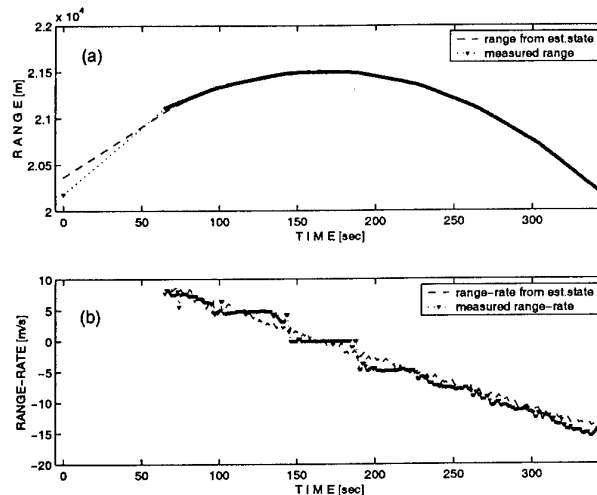


Figure 14: The measured range and range-rate against what would have been measured, had the MLE estimated target state been correct

11. N. J. Gordon, D. J. Salmond, and A. F. M. Smith. Novel approach to nonlinear/non-Gaussian bayesian state estimation. *IEE Proc.-F*, 140(2):107–113, 1993.
12. F. A. Graybill. *Theory and Application of the linear model*. Duxbury Press, Belmont, CA, 1976.
13. A. H. Jazwinski. *Stochastic Processes and Filtering Theory*. Academic Press, 1970.
14. D. Lerro and Y. Bar-Shalom. Tracking with debiased consistent converted measurements versus EKF. *IEEE Trans. Aerospace and Electronic Systems*, 29(3):1015–1022, July 1993.
15. J. McCarthy. Design and implementation of Ingara Radar Scan Modes. Technical report, DSTO, Australia, May 2000. In Review.
16. C. Musso, N. Oudjane, and F. LeGland. Improving regularised particle filters. In A. Doucet, N. deFreitas, and N. J. Gordon, editors, *Sequential Monte Carlo methods in Practice*. Springer-Verlag, New York, 2001.
17. N. Peach. Bearings-only tracking using a set of range-parametrised extended Kalaman filters. *IEE Proc. Control Theory Appl.*, 142(1):73–80, Jan. 1995.
18. W. H. Press, B. P. Flannery, S. A. Teukolsky, and W. T. Vetterling. *Numerical recipes in C*. Cambridge Univ. Press, 1988.
19. T. L. Song. Observability of target tracking with range-only measurements. *IEEE Journal of Oceanic Engineering*, 24:383–387, July 1999.
20. H. L. VanTrees. *Detection, Estimation and Modulation Theory (Part I)*. John Wiley & Sons, 1968.
21. D. R. Wehner. *High-Resolution Radar*. Artech House, 2nd edition, 1995.

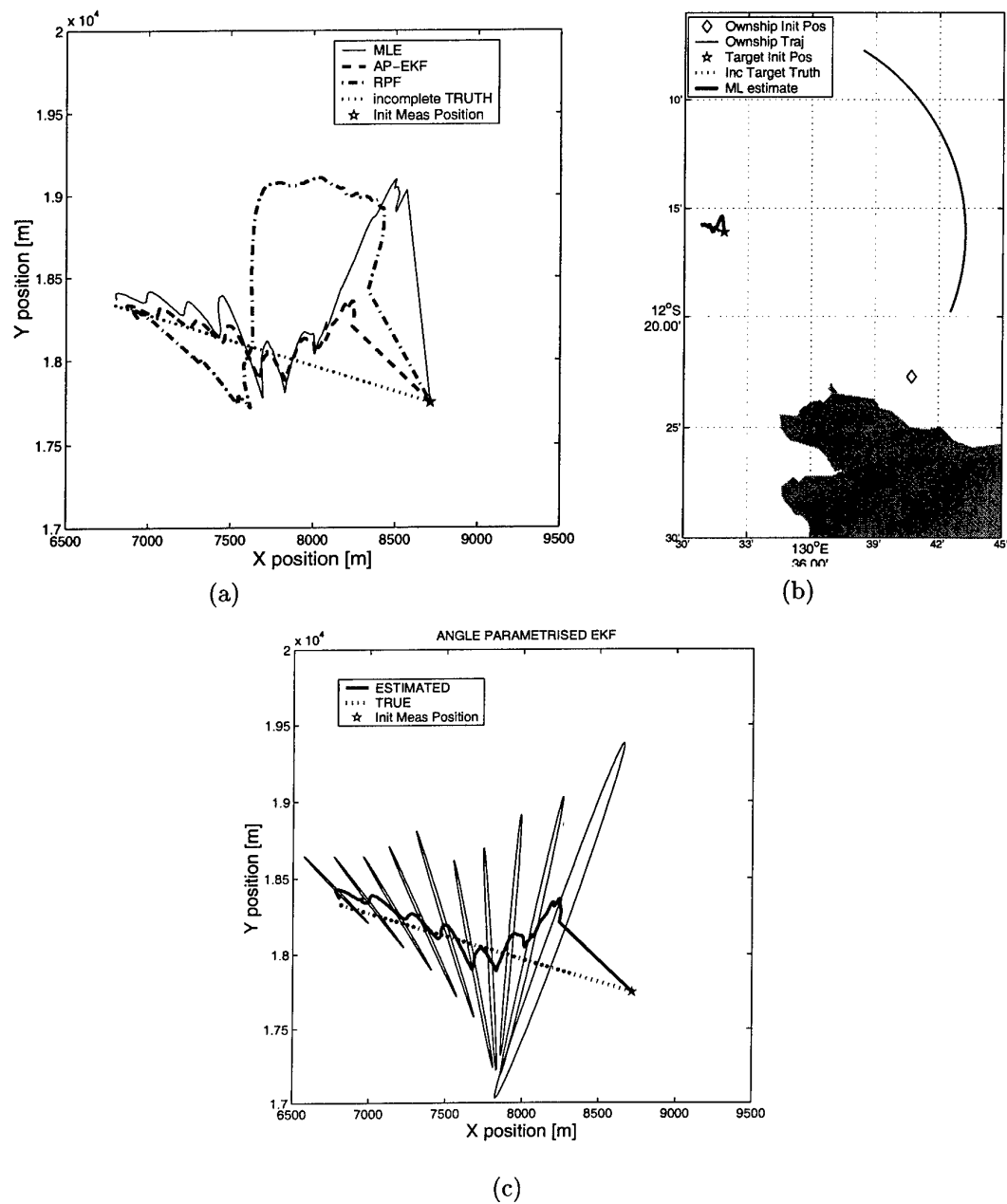


Figure 15: Estimated target trajectories: (a) local Cartesian coordinates; (b) geographic map; (c) AP-EKF with uncertainty ellipses (local coordinates)

DISTRIBUTION LIST

Target Motion Analysis Using Range-Only Measurements: Algorithms, Performance and Application to Ingara ISAR Data

B. Ristic, S. Arulampalam and J. McCarthy

Number of Copies

DEFENCE ORGANISATION

Task Sponsor

Director General Aerospace Development	1
--	---

S&T Program

Chief Defence Scientist	1
FAS Science Policy	1
AS Science Corporate Management	1
Director General Science Policy Development	1
Counsellor, Defence Science, London	Doc Data Sht
Counsellor, Defence Science, Washington	Doc Data Sht
Scientific Adviser to MRDC, Thailand	Doc Data Sht
Scientific Adviser Policy and Command	1
Navy Scientific Adviser	Doc Data Sht
Scientific Adviser, Army	Doc Data Sht
Air Force Scientific Adviser	1
Director Trials	1

Aeronautical and Maritime Research Laboratory

Director, Aeronautical and Maritime Research Laboratory	1
---	---

Electronics and Surveillance Research Laboratory

Director, Electronics and Surveillance Research Laboratory	1
Chief, Surveillance Systems Division	1
Research Leader, WAS, SSD	1
Research Leader, TSR, SSD	1
Research Leader, IS, SSD	1
Dr John Percival, Head TSF, SSD	1
Dr Brett Haywood, Head MS, SSD	1
Authors	6

DSTO Research Library and Archives

Library Fishermans Bend	1
Library Maribyrnong	1
Library Salisbury	2

Australian Archives	1
Library, MOD, Pyrmont	Doc Data Sht
Library, MOD, HMAS Stirling	1
US Defense Technical Information Center	2
UK Defence Research Information Centre	2
Canada Defence Scientific Information Service	1
NZ Defence Information Centre	1
National Library of Australia	1
Capability Systems Staff	
Director General Maritime Development	Doc Data Sht
Director General Land Development	Doc Data Sht
Director General ISREW	Doc Data Sht
Navy	
SO(Science), Director of Naval Warfare, Maritime Headquarters Annex, Garden Island	Doc Data Sht
Army	
ABCA Standardisation Officer, Puckapunyal	4
SO(Science), DJFHQ(L), MILPO, Enoggera, Queensland 4057	Doc Data Sht
Air Force	
Intelligence Program	
DGSTA, Defence Intelligence Organisation	1
Manager, Information Centre, Defence Intelligence Organisation	1
Acquisitions Program	
Corporate Support Program	
Library Manager, DLS Canberra	1
UNIVERSITIES AND COLLEGES	
Prof. Rob Evans, Dept. EEE, The University of Melbourne	1
Australian Defence Force Academy Library	1
Head of Aerospace and Mechanical Engineering, ADFA	1
Deakin University Library, Serials Section (M List)	1
Hargrave Library, Monash University	Doc Data Sht
Librarian, Flinders University	1
OTHER ORGANISATIONS	
NASA (Canberra)	1

AusInfo	1
State Library of South Australia	1
Parliamentary Library of South Australia	1
ABSTRACTING AND INFORMATION ORGANISATIONS	
Library, Chemical Abstracts Reference Service	1
Engineering Societies Library, US	1
Materials Information, Cambridge Scientific Abstracts, US	1
Documents Librarian, The Center for Research Libraries, US	1
INFORMATION EXCHANGE AGREEMENT PARTNERS	
Acquisitions Unit, Science Reference and Information Service, UK	1
Library - Exchange Desk, National Institute of Standards and Technology, US	1
National Aerospace Laboratory, Japan	1
National Aerospace Laboratory, Netherlands	1
SPARES	
DSTO Salisbury Research Library	5
Total number of copies:	62

DEFENCE SCIENCE AND TECHNOLOGY ORGANISATION DOCUMENT CONTROL DATA				1. CAVEAT/PRIVACY MARKING	
2. TITLE Target Motion Analysis Using Range-Only Measurements: Algorithms, Performance and Application to Ingara ISAR Data			3. SECURITY CLASSIFICATION Document (U) Title (U) Abstract (U)		
4. AUTHORS B. Ristic, S. Arulampalam and J. McCarthy			5. CORPORATE AUTHOR Electronics and Surveillance Research Laboratory PO Box 1500 Salisbury, South Australia, Australia 5108		
6a. DSTO NUMBER DSTO-TR-1095		6b. AR NUMBER AR-011-693		6c. TYPE OF REPORT Technical Report	
7. DOCUMENT DATE January 2001					
8. FILE NUMBER	9. TASK NUMBER SSD Support to AIR 5276	10. SPONSOR		11. No OF PAGES 29	12. No OF REFS 21
13. URL OF ELECTRONIC VERSION http://www.dsto.defence.gov.au/corporate/reports/DSTO-TR-1095.pdf			14. RELEASE AUTHORITY Chief, Surveillance Systems Division		
15. SECONDARY RELEASE STATEMENT OF THIS DOCUMENT <i>Approved For Public Release</i> OVERSEAS ENQUIRIES OUTSIDE STATED LIMITATIONS SHOULD BE REFERRED THROUGH DOCUMENT EXCHANGE, PO BOX 1500, SALISBURY, SOUTH AUSTRALIA 5108					
16. DELIBERATE ANNOUNCEMENT No Limitations					
17. CITATION IN OTHER DOCUMENTS No Limitations					
18. DEFTEST DESCRIPTORS Target tracking range-only measurements Cramer-Rao bounds particle filter					
19. ABSTRACT The report considers the problem of target motion analysis from range and range-rate target measurements. The motivation for this work comes from the need to track the target motion with the Ingara Multi-Mode Radar during an extended data collection in the ISAR mode. The report makes three main contributions. First, the theoretical Cramér-Rao bound for the performance of an unbiased range-only tracking algorithm is derived. Second, three algorithms for target motion analysis (using range and range-rate measurements only) are developed and compared to the theoretical bounds of performance. The three algorithms are: the Maximum Likelihood estimator, the Extended Kalman filter and the Regularised Particle filter. Finally, the report presents the results of the application of the developed theory to the ISAR data collected in the recent trials with the Ingara radar.					